Supplemental Information

Charge Carrier Dynamics Investigation of Dinitrogen to Ammonia by Photo-electrocatalytic Reduction via Cu_2S-In_2S_3 Heterostructure

This supplemental file includes:

- Supplemental Figure S1 to S46
- Supplemental Table S1 to S3

The sequence is the same as they are mentioned in the main text.

Supplemental Figures

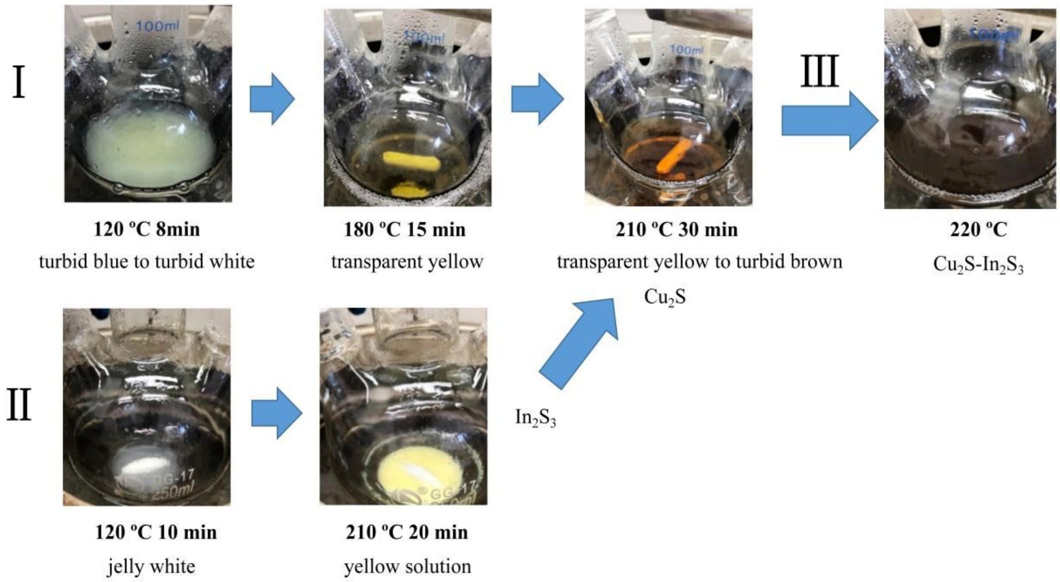

Figure S1. Schematic electronic photos for the synthesis of heterojunction catalysts.

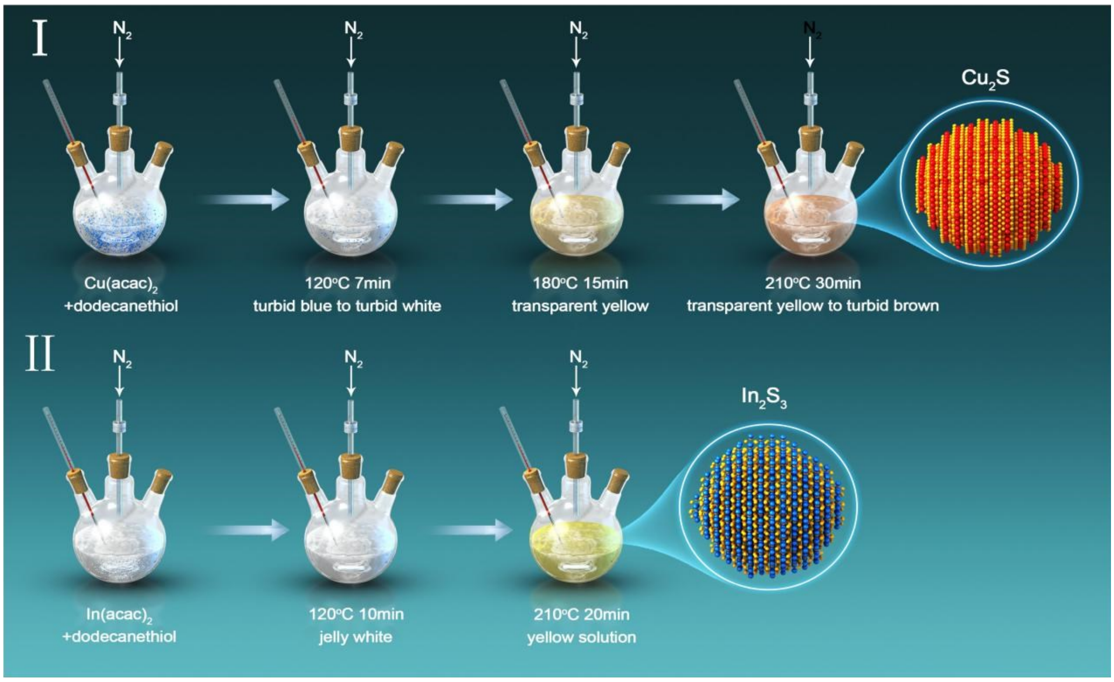

Figure S2. The schematic procedure of synthesizing Cu_2S and In_2S_3, respectively.

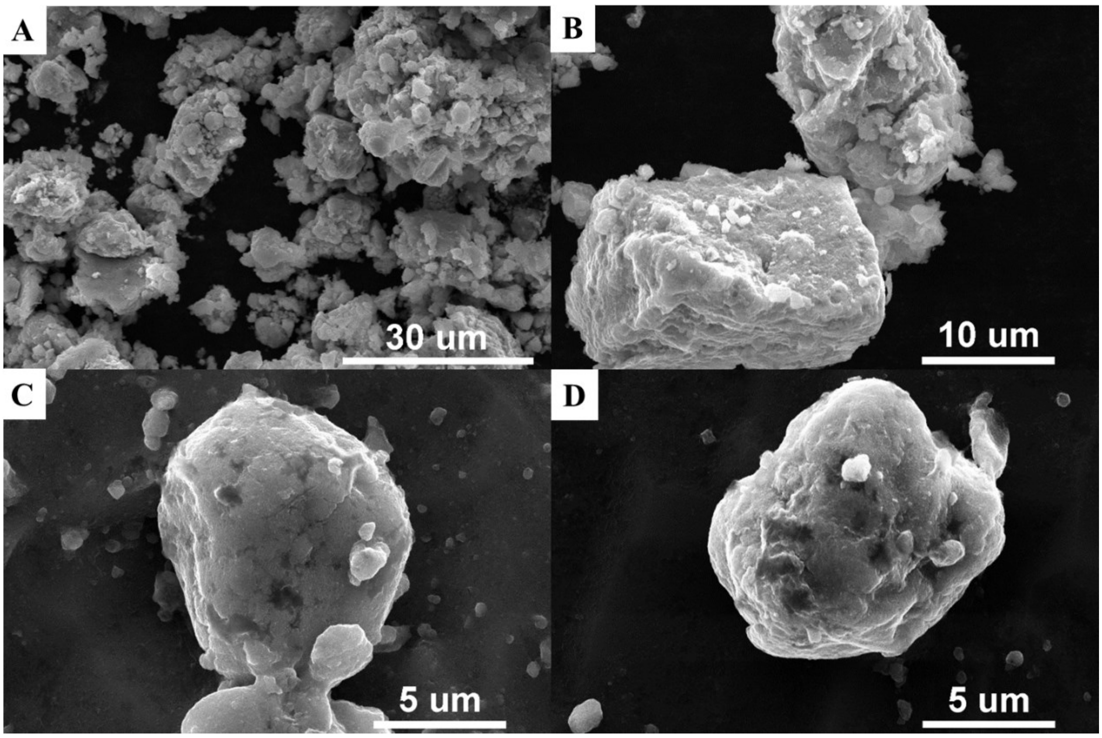

Figure S3. SEM images of Cu_2S-In_2S_3 heterostructure in different magnetic resolution.

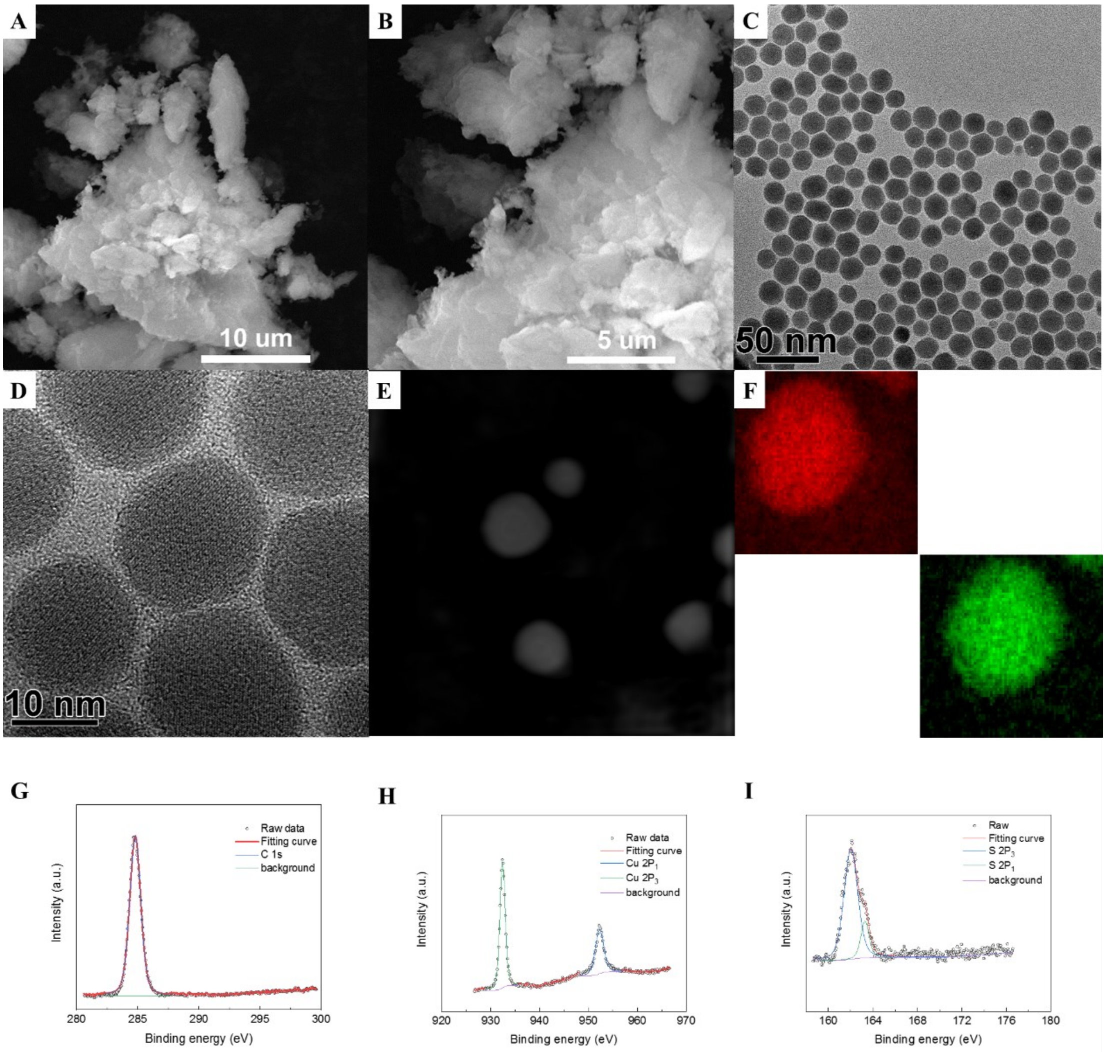

Figure S4. A), B) SEM images of Cu_2S sample in different magnetic resolution. C), D) TEM images of Cu_2S sample and E) The HAADF-STEM image. F) The corresponding mapping images of Cu_2S sample. G), H), I) XPS spectra of Cu_2S sample for Cu 2p and S 2p, respectively.

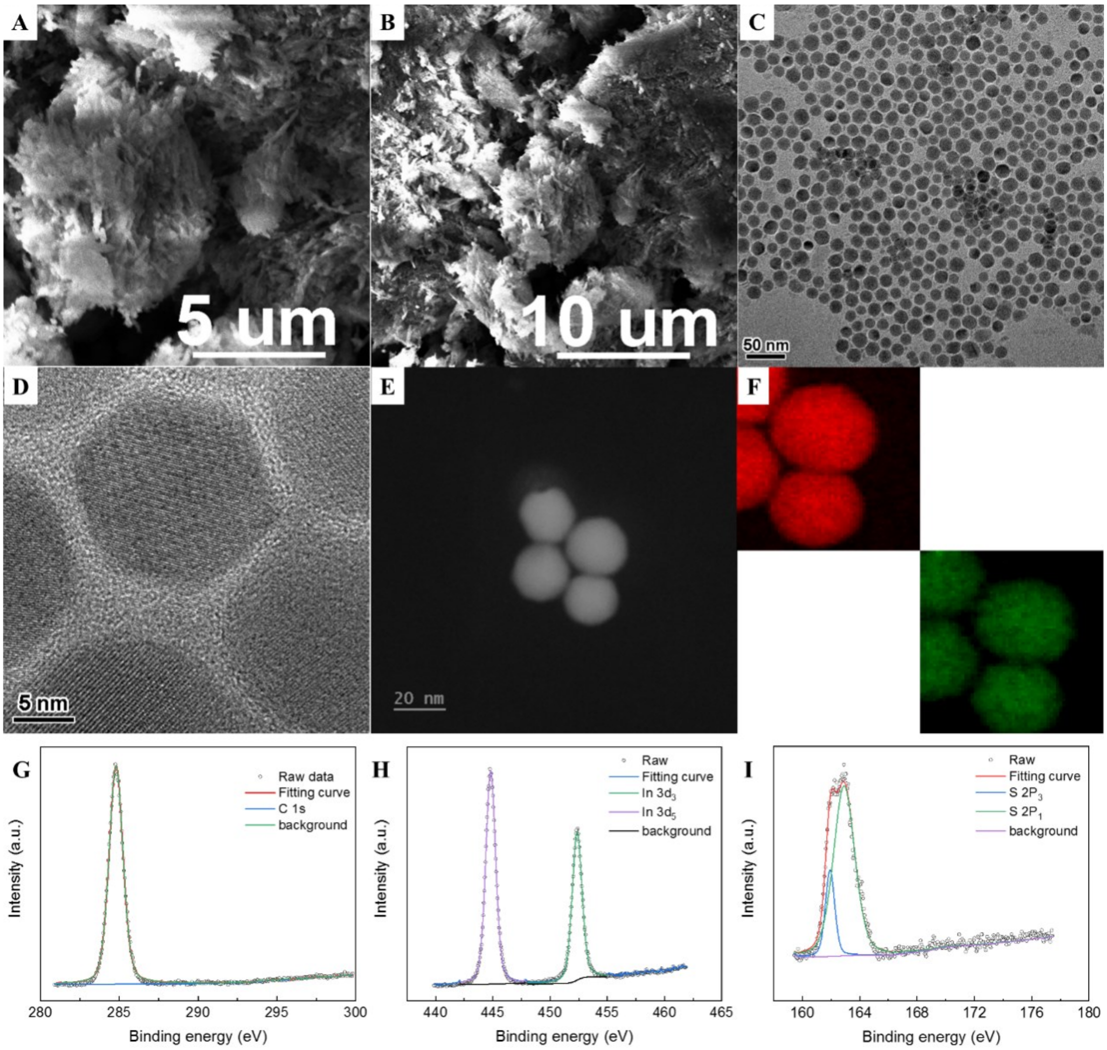

Figure S5. A), B) SEM images of In_2S_3 sample in different magnetic resolution. C), D) TEM images of In_2S_3 sample and E) The HAADF-STEM image. F) The corresponding mapping images of In_2S_3 sample. G), H), I) XPS spectra of In_2S_3 sample for In 3d and S 2p, respectively.

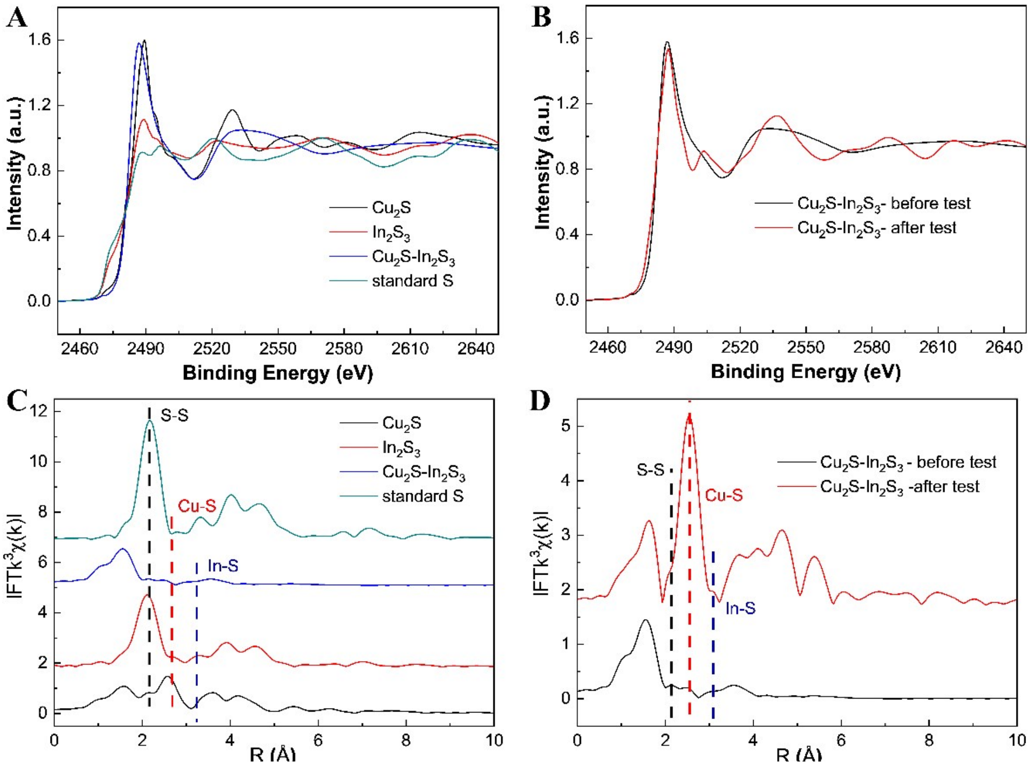

Figure S6. A) S K-edge XANES spectra of Cu_2S, In_2S_3, Cu_2S-In_2S_3, and S powder. B) S K-edge XANES spectra of Cu_2S-In_2S_3 before and after reaction. C) EXAFS in *R*-space for the Cu_2S, In_2S_3, Cu_2S-In_2S_3, and S powder. D) EXAFS in *R*-space for the Cu_2S-In_2S_3 before and after reaction.

The Fourier transformed (FT) *k*3-weighted (*k*)-function of the EXAFS spectra in *R*-space suggested the S species were Cu-S, In-S and S-S, in the samples. The peak at ≈2.45 Å is attributed to the Cu-S in Cu_2S, Cu_2S-In_2S_3 and the peak ≈3.43 Å is ascribed to the In-S in In_2S_3, Cu_2S-In_2S_3, whereas the peak at ≈2.08 Å suggested the S-S in Cu_2S-In_2S_3.

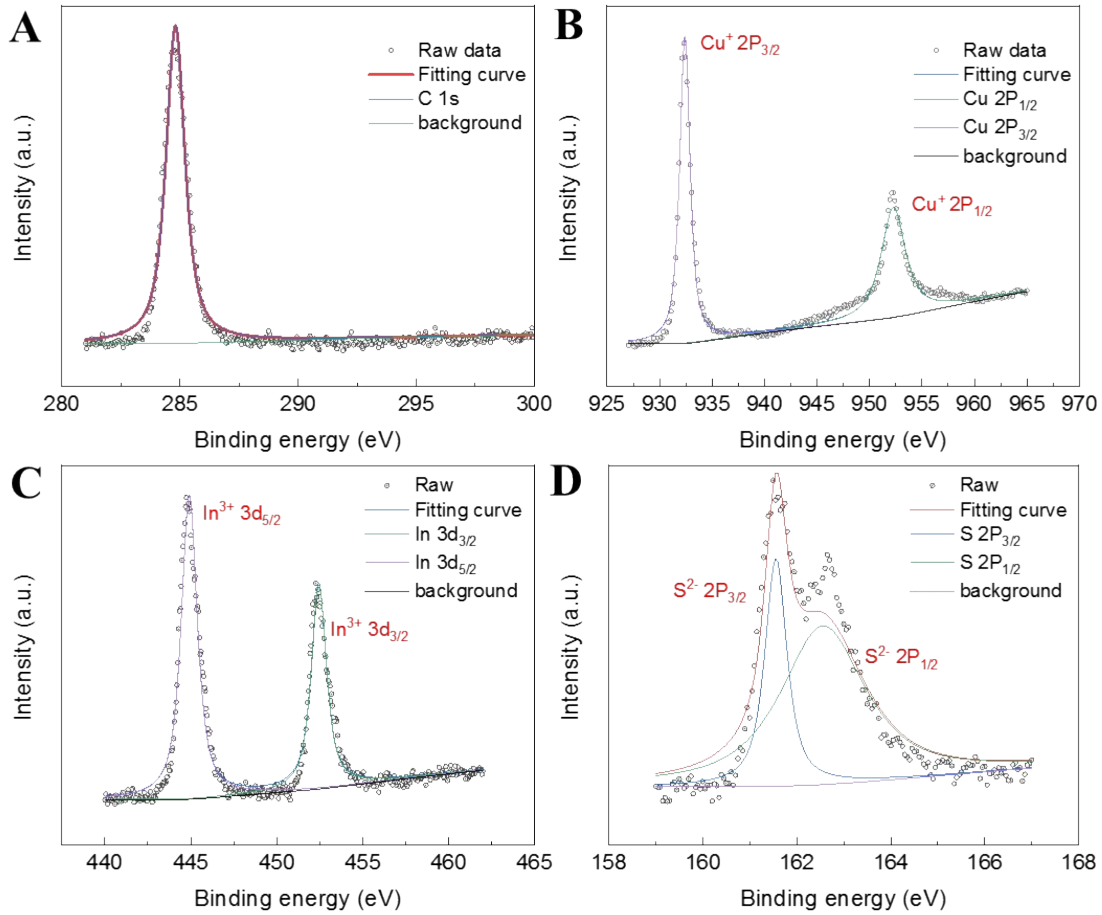

Figure S7. XPS spectra of Cu_2S-In_2S_3 sample for B) Cu 2p, C) In 3d and D) S 2p, respectively.

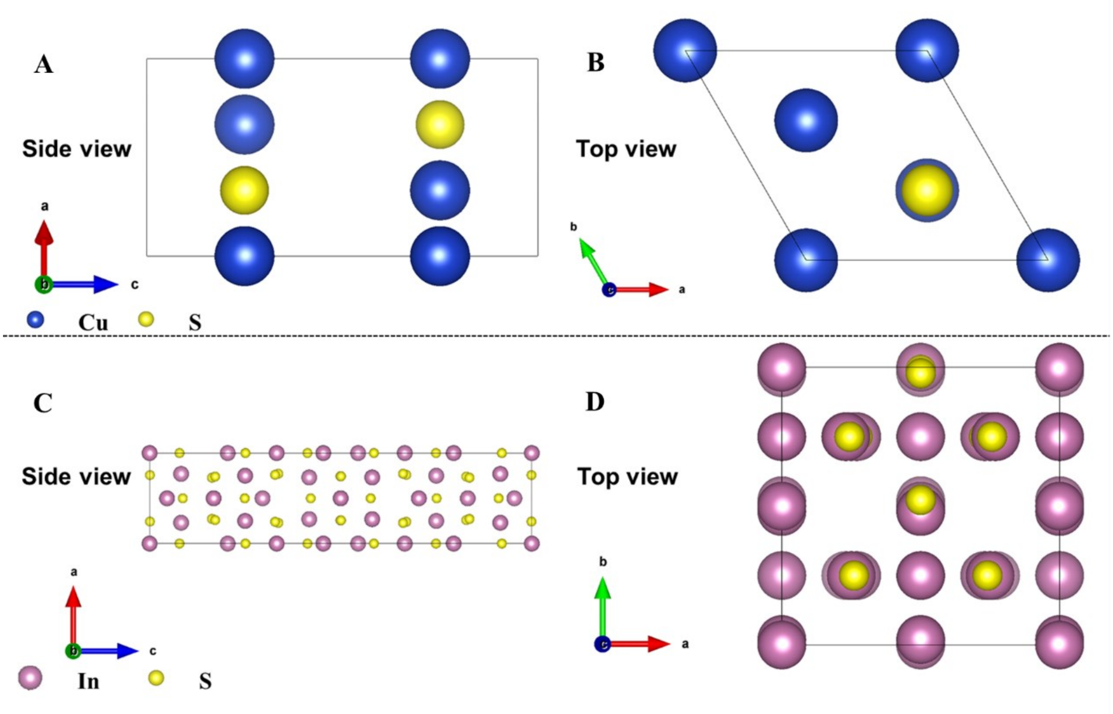

Figure S8. Schematic models for Cu_2S A) side view and B) top view. In_2S_3 C) side view and D) top view.

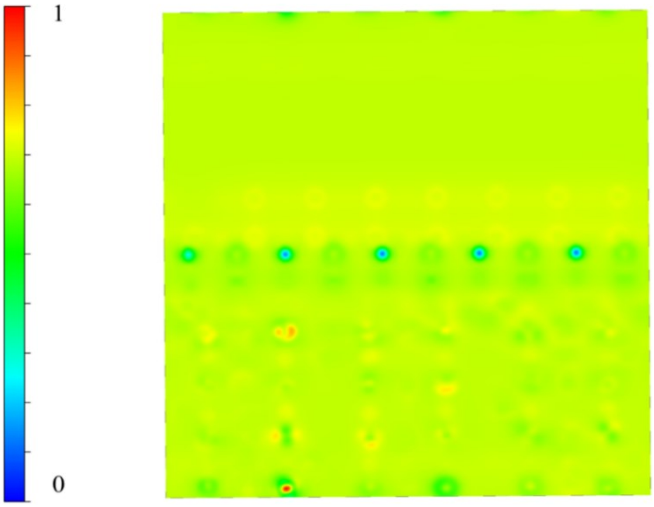

Figure S9. Schematic graph of the build-in electric field formed by the electron transfers from In_2S_3 to Cu_2S as the 2D.

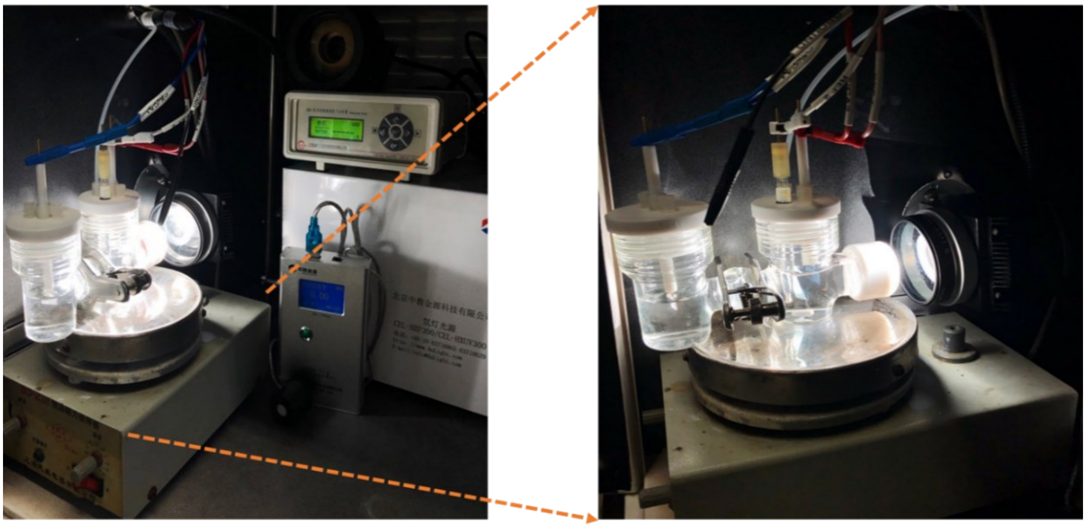

Figure S10. Photograph of the testing conditions.

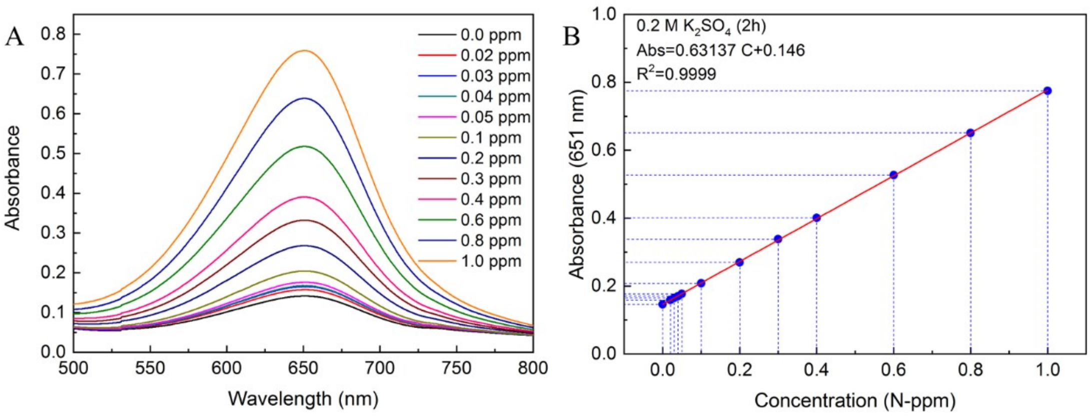

Figure S11. A) UV-Vis curves of indophenol assays with NH_4^+ ions after incubated for 2 h at room temperature, B) Calibration curve used for calculation of NH_3 concentrations.

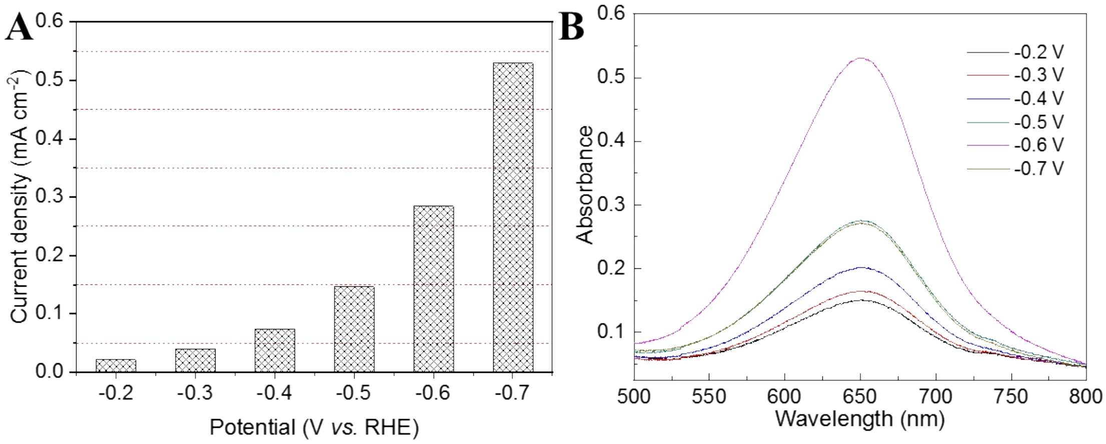

Figure S12. A) The current densities for Cu_2S-In_2S_3 electrolyzed at different applied potentials under one sunlight. B) UV-Vis curves of indophenol assays with NH_4^+ ions for Cu_2S-In_2S_3 electrolyzed at different applied potentials after incubated for 2 h at room temperature.

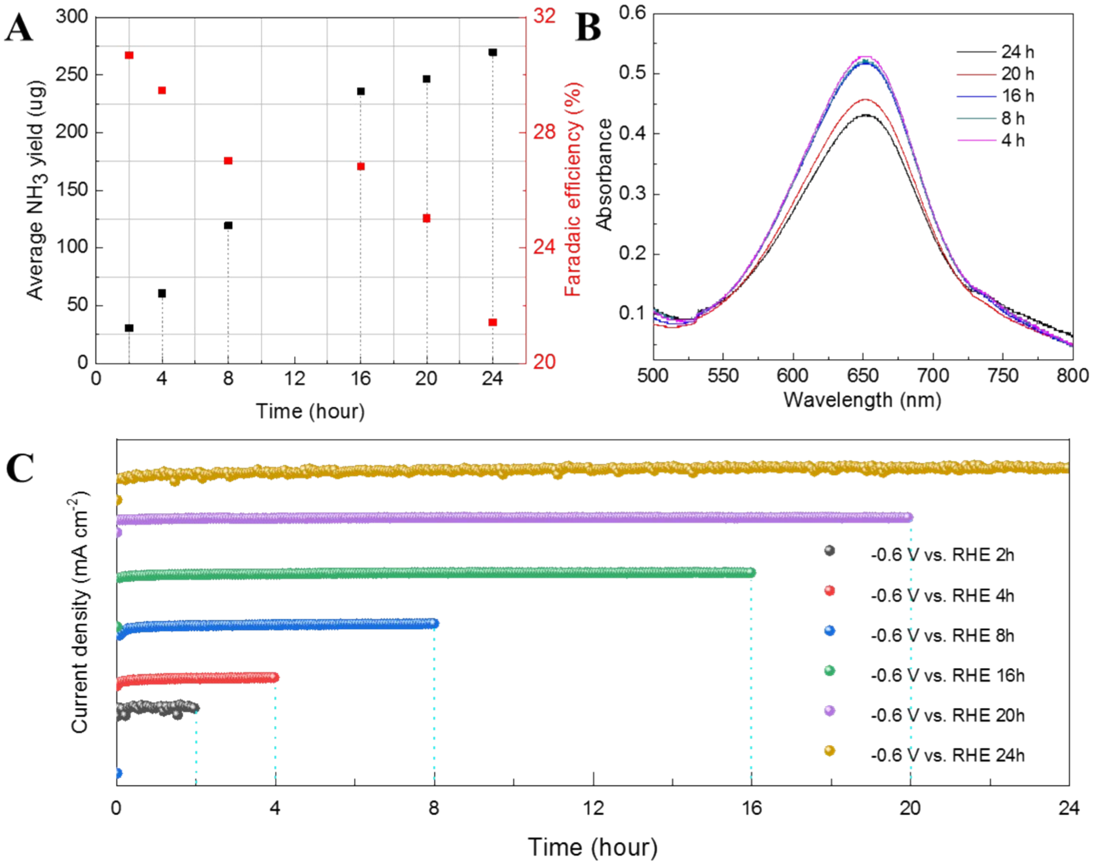

Figure S13. A) The average NH_3 yields and faradaic efficiency under different reaction time. B) The corresponding UV-Vis curves of indophenol assays with NH_4^+ ions for Cu_2S-In_2S_3 electrolyzed under different reaction time after incubated for 2 h at room temperature. C) The current density stability test under different reaction time.

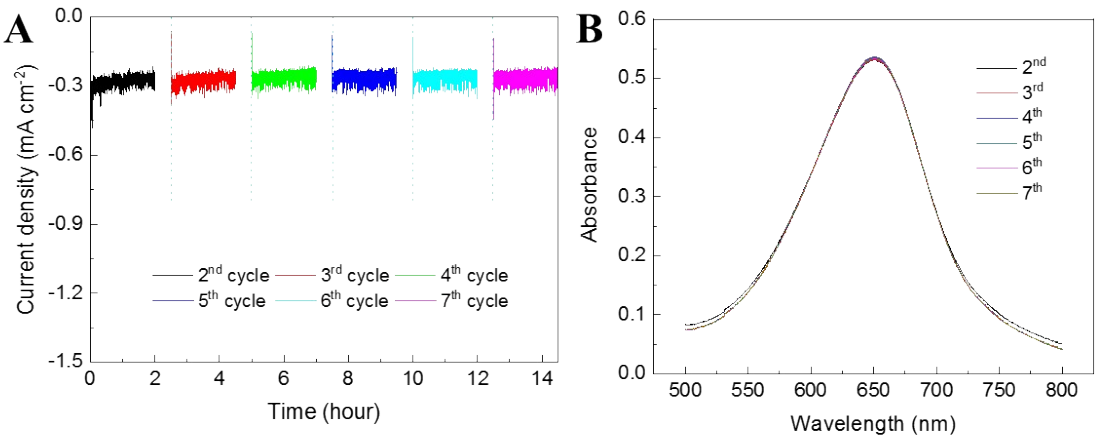

Figure S14. A) The average NH_3 yields and faradaic efficiency under different cycle test. B) The corresponding UV-Vis curves of indophenol assays with NH_4^+ ions for Cu_2S-In_2S_3 electrolyzed under different cycles after incubated for 2 h at room temperature.

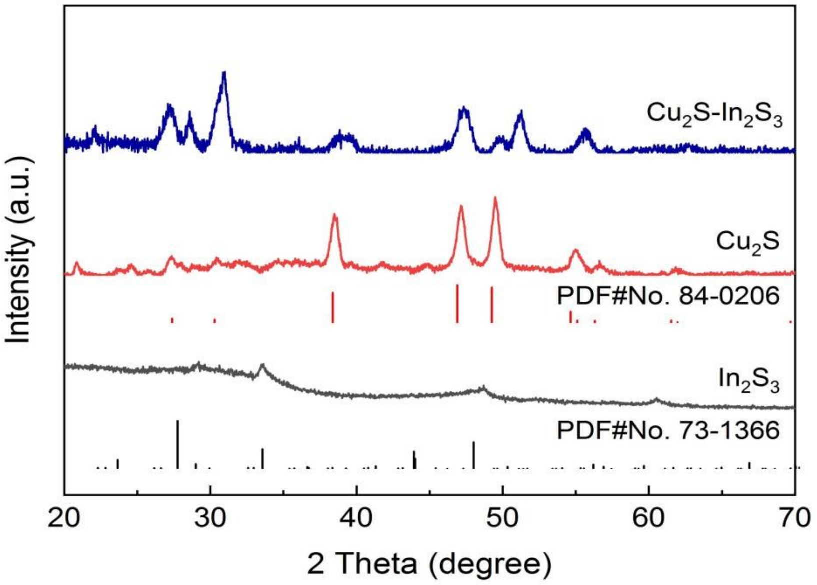

Figure S15. XRD spectra of Cu_2S-In_2S_3 heterostructure, Cu_2S and In_2S_3 catalyst after reaction.

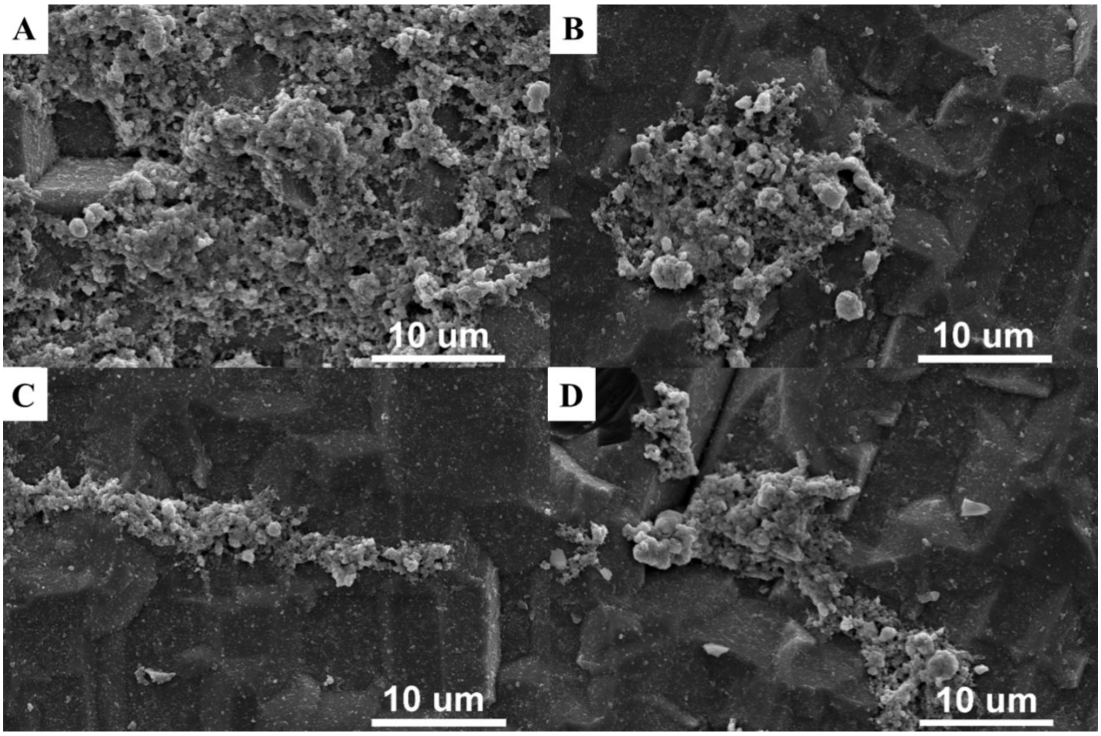

Figure S16. SEM images of Cu_2S-In_2S_3 heterostructure catalyst after reaction.

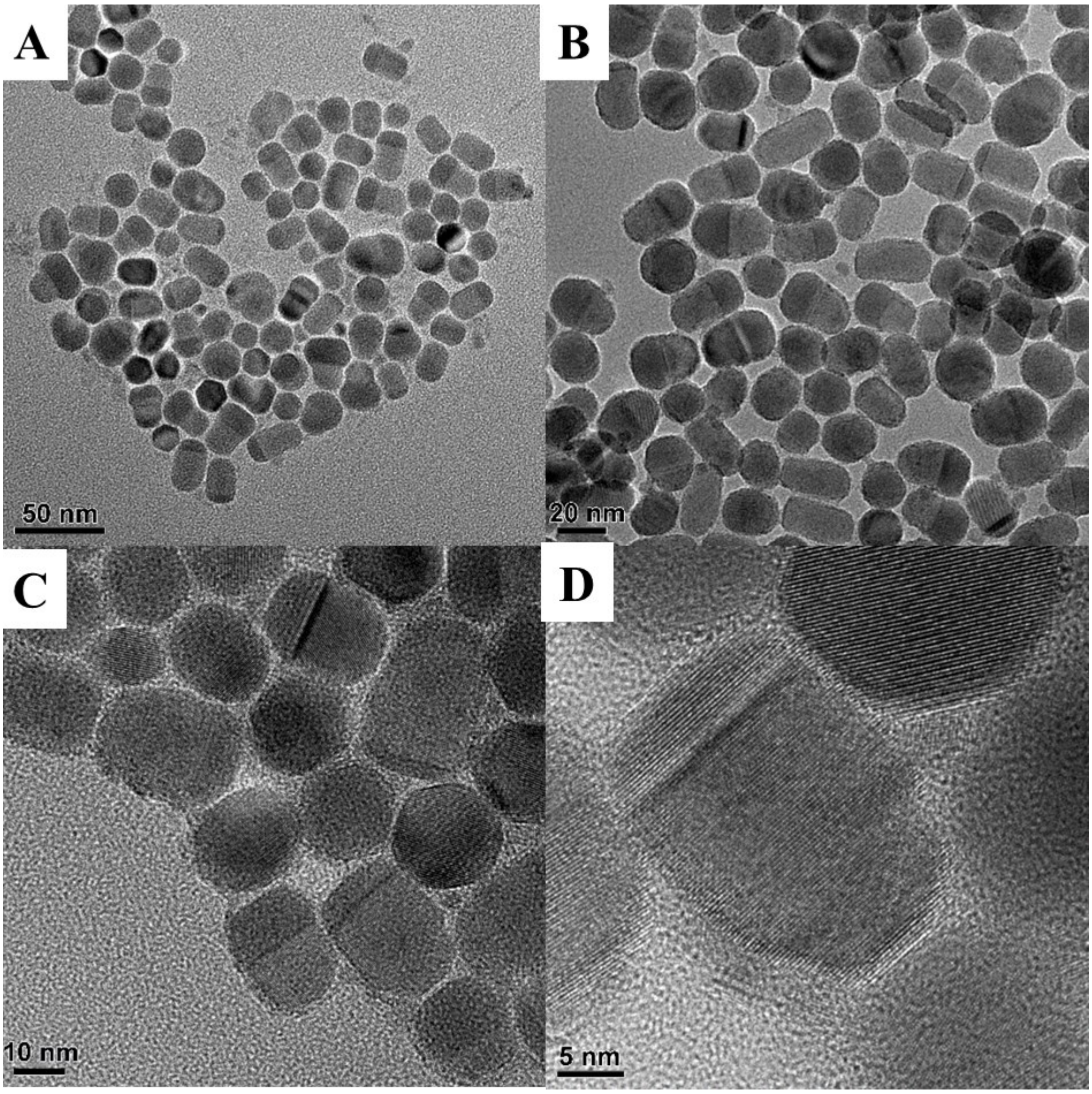

Figure S17. TEM images of Cu_2S-In_2S_3 heterostructure catalyst after reaction.

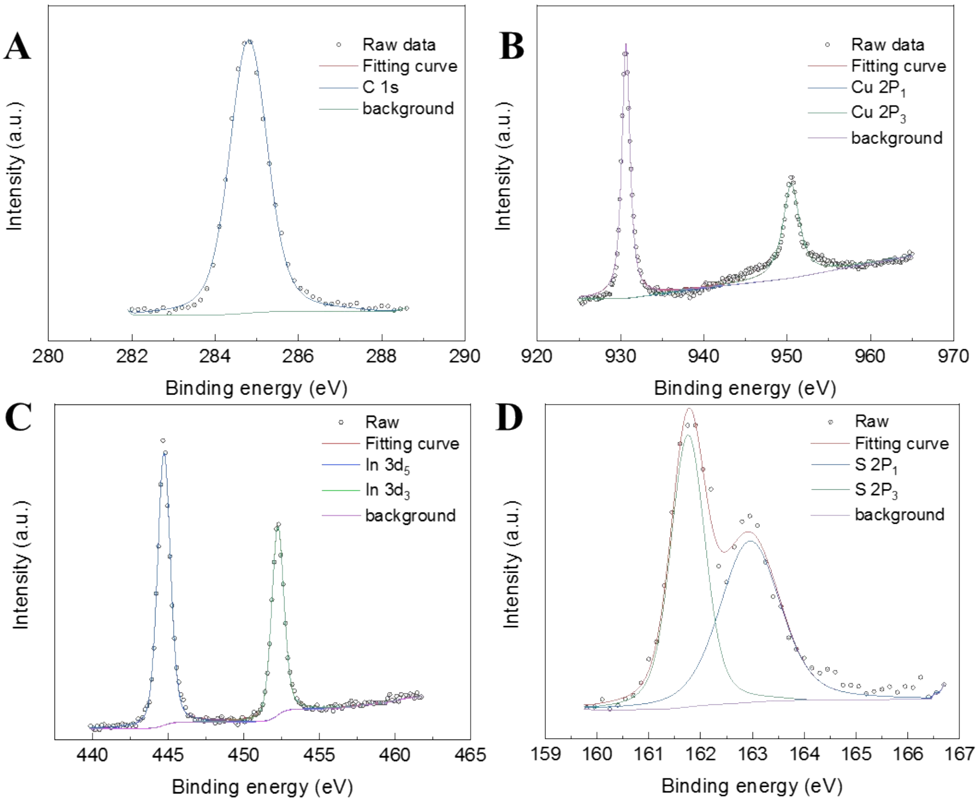

Figure S18. XPS spectra of Cu_2S-In_2S_3 heterostructure catalyst after reaction.

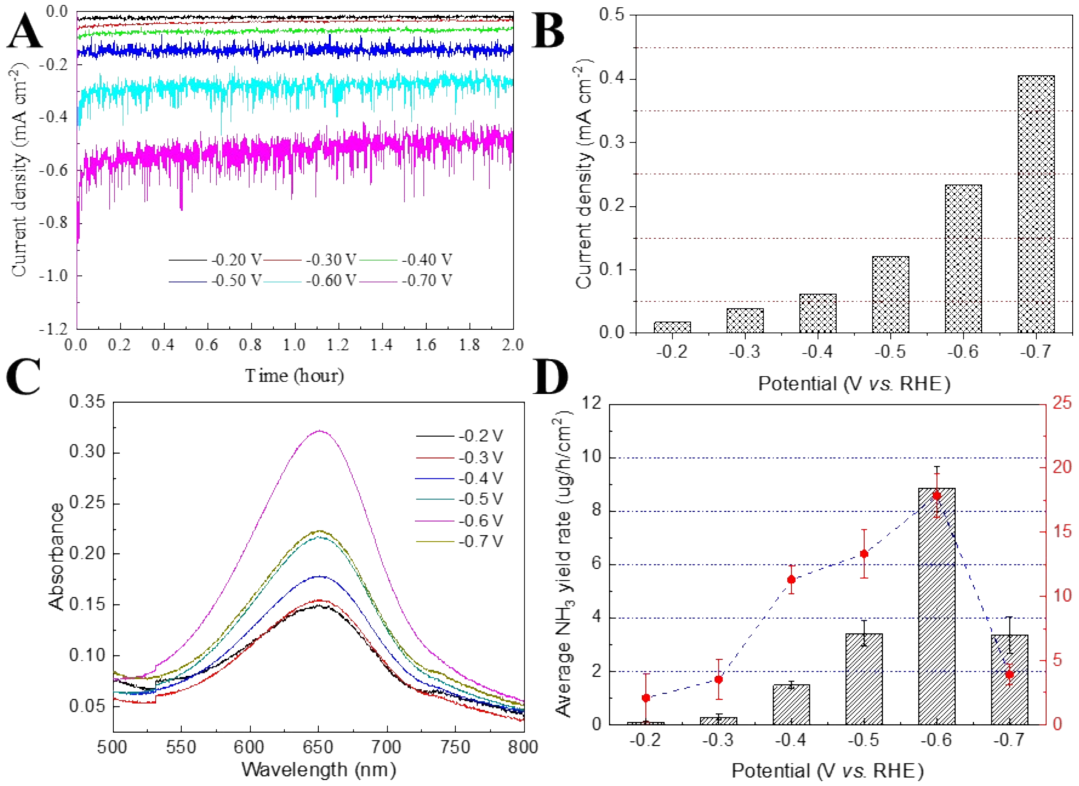

Figure S19. A) Chrono-amperometry results at the corresponding potentials. B) The current densities for Cu_2S electrolyzed at different applied potentials under one sunlight. C) UV-Vis curves of indophenol assays with NH_4^+ ions for Cu_2S electrolyzed at different applied potentials after incubated for 2 h at room temperature. D) Yield rates of NH_3 (black bar) and Faradaic efficiencies (red point) at each given potential for Cu_2S catalyst.

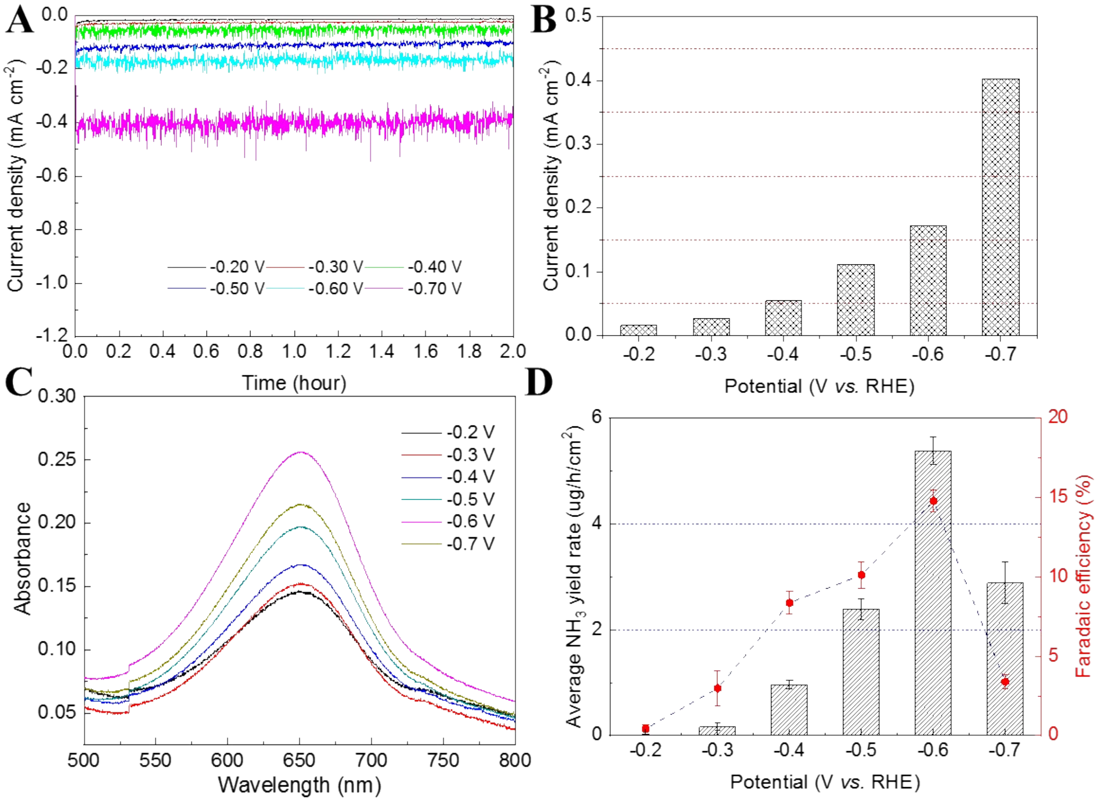

Figure S20. A) Chrono-amperometry results at the corresponding potentials. B) The current densities for In_2S_3 electrolyzed at different applied potentials under one sunlight. C) UV-Vis curves of indophenol assays with NH_4^+ ions for In_2S_3 electrolyzed at different applied potentials after incubated for 2 h at room temperature. D) Yield rates of NH_3 (black bar) and Faradaic efficiencies (red point) at each given potential for In_2S_3 catalyst.

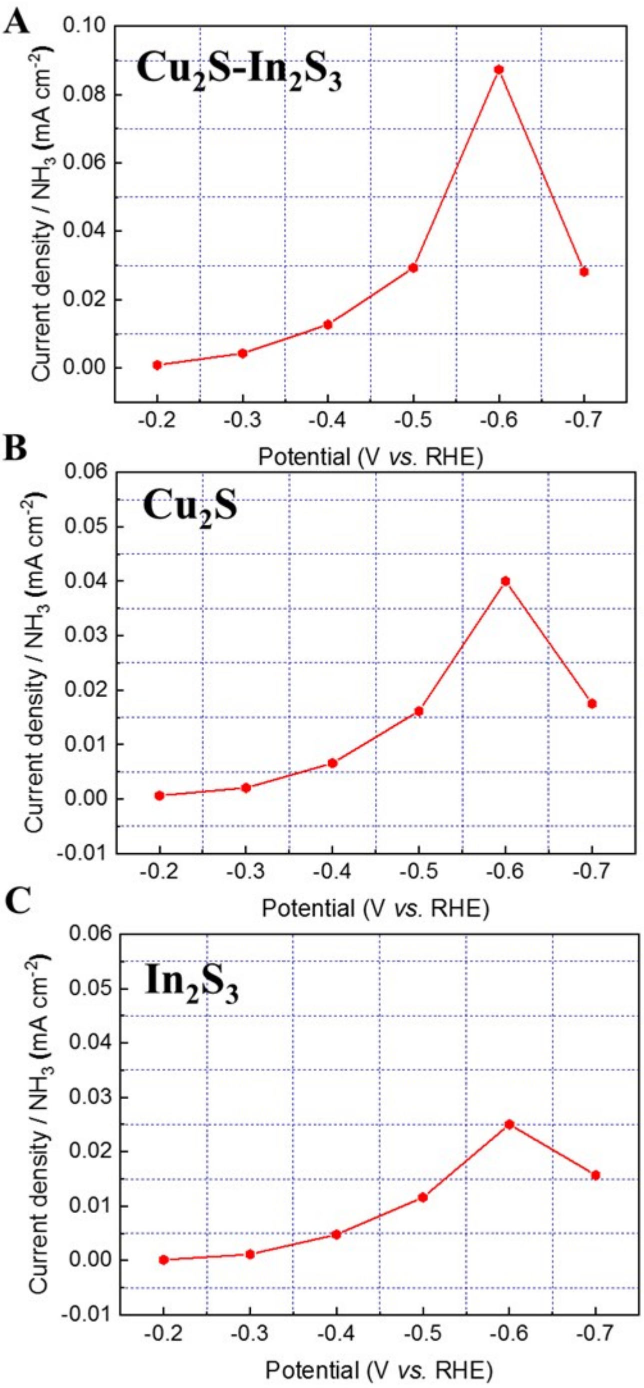

Figure S21. The current densities of Cu_2S-In_2S_3 heterostructure, Cu_2S and In_2S_3 catalysts for producing ammonia at different applied potential under one sunlight.

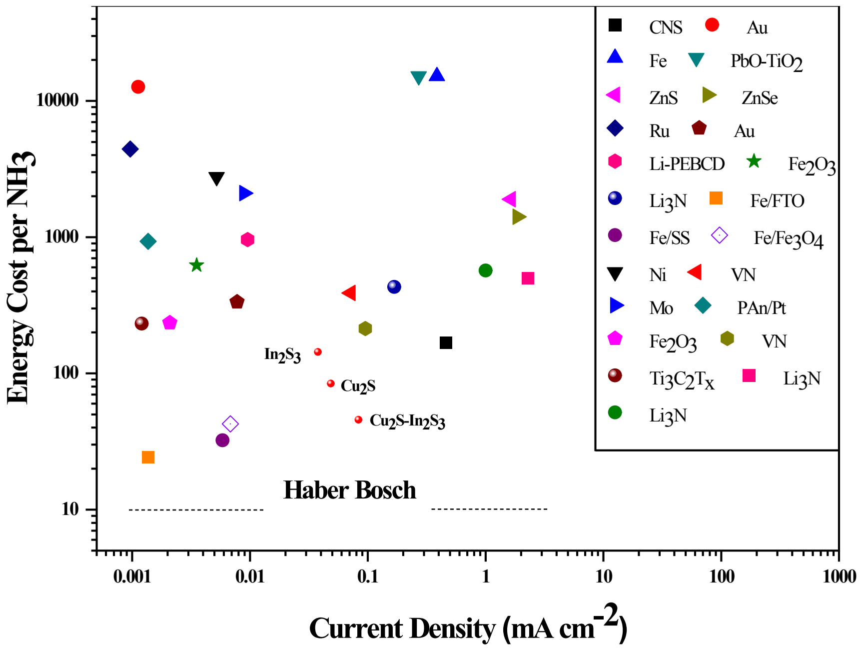

Figure S22. The energy cost per NH_3 at the obtained current density for the reported catalysts[1].

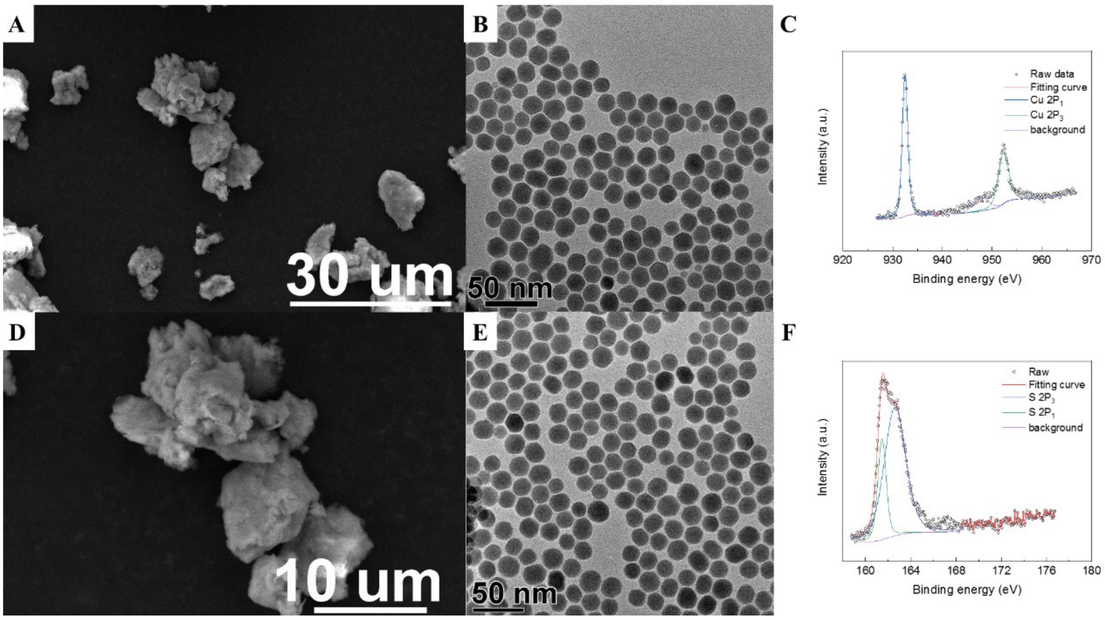

Figure S23. A) and B) SEM images of Cu_2S catalyst after reaction. C) and D) TEM images of Cu_2S catalyst after reaction. E) and F) XPS spectra of Cu_2S catalyst after reaction.

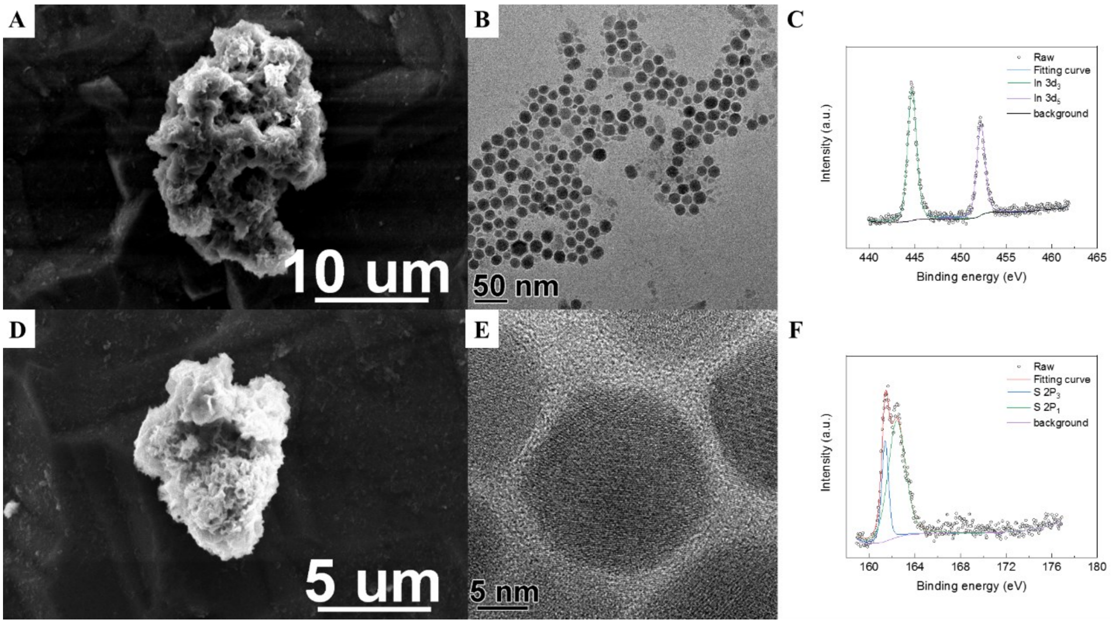

Figure S24. A) and B) SEM images of In_2S_3 catalyst after reaction. C) and D) TEM images of In_2S_3 catalyst after reaction. E) and F) XPS spectra of In_2S_3 catalyst after reaction.

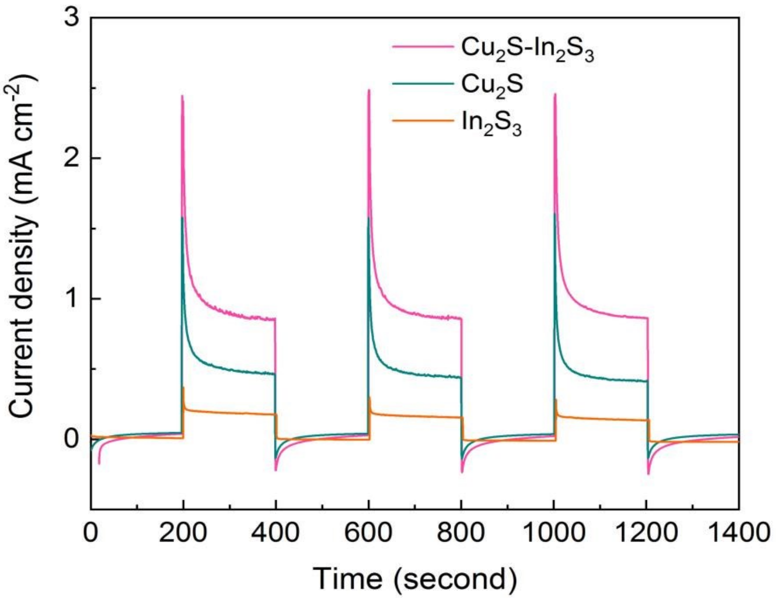

Figure S25. Transient photocurrent responses under repeated on-off cycles for Cu_2S-In_2S_3 heterostructure, Cu_2S and In_2S_3 catalysts.

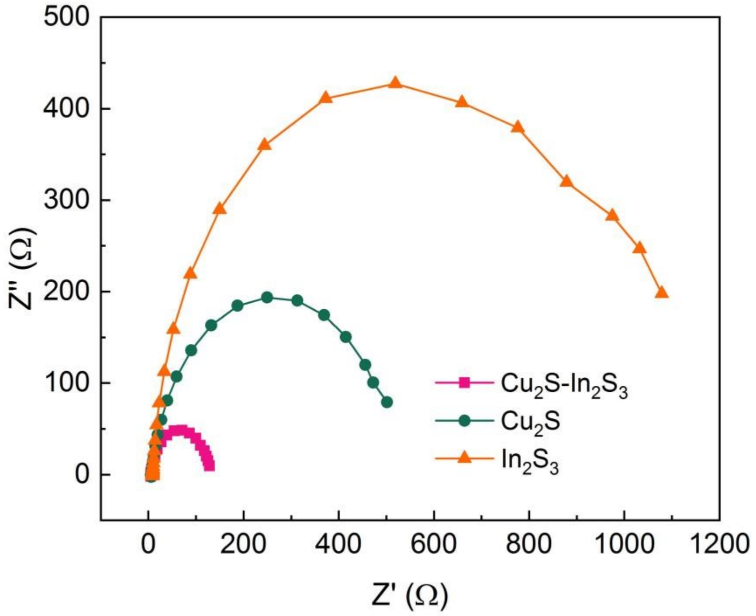

Figure S26. Electrochemical impedance spectra (EIS) for Cu_2S-In_2S_3 heterostructure, Cu_2S and In_2S_3 catalysts.

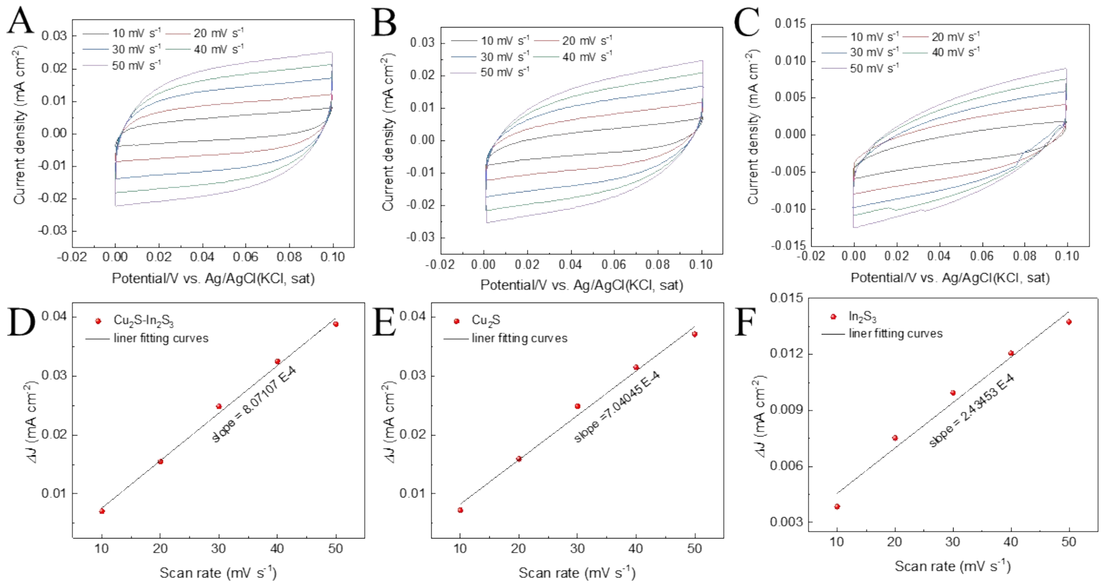

Figure S27. Electrochemical surface area measurement of the samples using double-layer capacitance. Cyclic voltammogram scans taken over a range of scan rates in the potential window with mainly double-layer charging and discharging: A) Cu_2S-In_2S_3 heterostructure, B) Cu_2S and C) In_2S_3. D), E) and F) Double-layer charging current vs the scan rate, and the slope of the linear fit is double-layer capacitance.

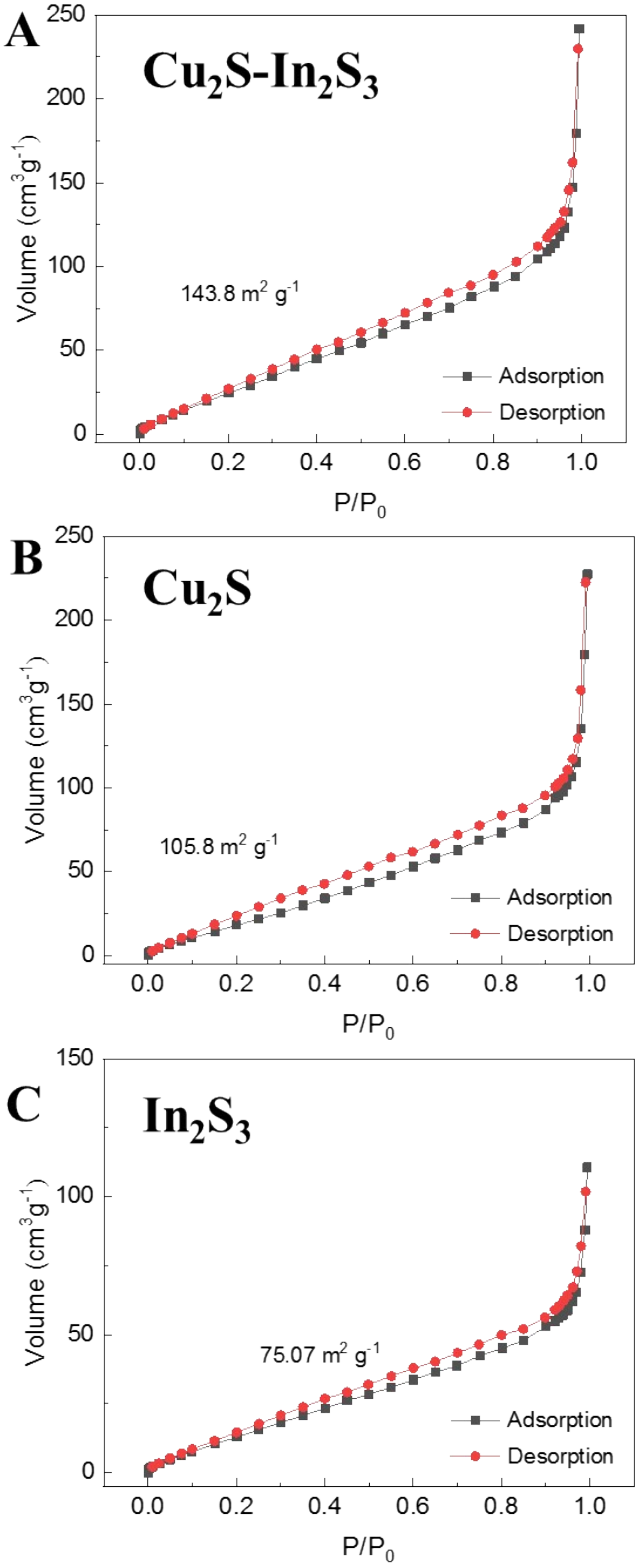

Figure S28. N_2 adsorption-desorption measurements for Cu_2S-In_2S_3 heterostructure, Cu_2S and In_2S_3.

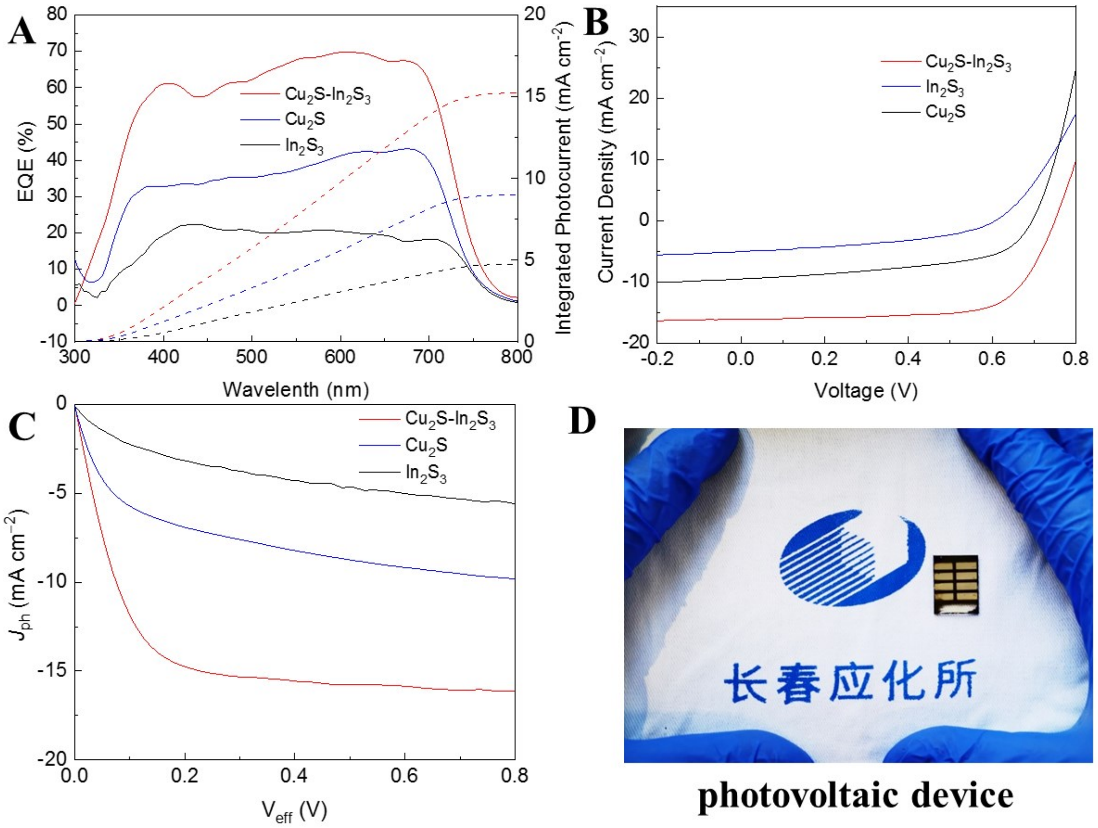

Figure S29. Photovoltaic device performance of Cu_2S-In_2S_3 heterostructure, Cu_2S and In_2S_3. A) EQE spectra and integrated current of devices. B) *J-V* curves of champion devices under AM 1.5 G illumination at a scan rate of 0.02 V s^{-1} scanning. C) J_{ph} vs. V_{eff} curves. D) Schematic illustration of the device.

The obtained *J-V* curves of Cu_2S, In_2S_3 and Cu_2S-In_2S_3 are scanned under AM 1.5 G illumination at a scan rate of 0.02 V s^{-1} in a N_2-filled glove box, and the statistics of the photovoltaic parameters of these three devices are summarized in **Figure S29A** and **Table S3**. The results of open-circuit voltage (V_{oc}), short-circuit current (J_{sc}), fill factor (*FF*), and PCE of devices are listed in Supplementary Table 3. The open-circuit voltage (V_{oc}) only decreases to 0.61 V (In_2S_3) and 0.70 V (Cu_2S) from 0.75 V (Cu_2S-In_2S_3) and the corresponding variance percentages are 22.9% and 7.1%, respectively. And the short-circuit current (J_{sc}) increased about 2.2 and 0.69 times, respectively, apparently improves from 5.02 mA cm^{-2} (In_2S_3) and 9.52 mA cm^{-2} (Cu_2S) to 16.10 mA cm^{-2} (Cu_2S-In_2S_3), indicating that the fabrication of heterojunction would obviously improve the short circuit current. Meanwhile, the fill factor (*FF*) also become better. For the control devices, PCE obtained under *J-V* curves scanning were 1.29% and 3.53%, excitingly, the PCE of Cu_2S-In_2S_3s device significantly increased owing to the simultaneously improved V_{oc}, J_{sc}, and *FF*, which could even reach a PCE of 8.31% with a V_{oc} of 0.75 V, a J_{sc} of 16.05 mA cm^{-2}, and an FF of 69%. **Figure S29B** is the external quantum efficiency (EQE) spectra of these three Cu_2S, In_2S_3 and Cu_2S-In_2S_3 devices, which shows significant improvement from 20% and 40 % to 75 %, owing to the improvement of free charge yield. In addition, the integrated photocurrent densities indicate the same trend and nearly same values with the short current observed in **Figure S29A**. **Figure S29C** shows net photocurrent density (J_{ph}) vsrsus effective voltage (V_{eff}) curves under AM 1.5 G illumination of the Cu_2S, In_2S_3 and Cu_2S-In_2S_3 devices, where $J_{ph} = J_L - J_d$ (J_L is the current density under AM 1.5 G illumination, J_d is the dark current density) and $V_{eff} = V_0 - V$ (V_0 is the voltage at which $J_{ph} = 0$, V is the applied bias voltage). As is known, J_{ph} versus V_{eff} curves illustrated the dependence of collected photogenerated charge carriers on internal electric field. In short-circuit condition (SCC), where V = 0 V, the Cu_2S, In_2S_3 and Cu_2S-In_2S_3 devices showed various V_{eff} of 0.6057 V, 0.6949 V and 0.7497 V, respectively, suggesting the fabrication of p-n heterojunction could generate bigger V_{bi}. As a result, the higher V_{eff} for the Cu_2S-In_2S_3 devices facilitated charge transport and collection, leading to larger J_{ph} and J_{sc}. In contrast, the Cu_2S and In_2S_3 device with lower V_{eff} gave smaller J_{ph} and J_{sc}. It is noted that the change in V_{bi} was in accordance with the V_{oc} results obtained from the *J*-*V* curves, suggesting that the enhanced V_{bi} could lead to a larger upper limit of V_{oc}. Overall, the enhanced V_{bi}, and improved charge collection of the Cu_2S-In_2S_3 devices have led to significant improvement in photovoltaic parameters.[2]

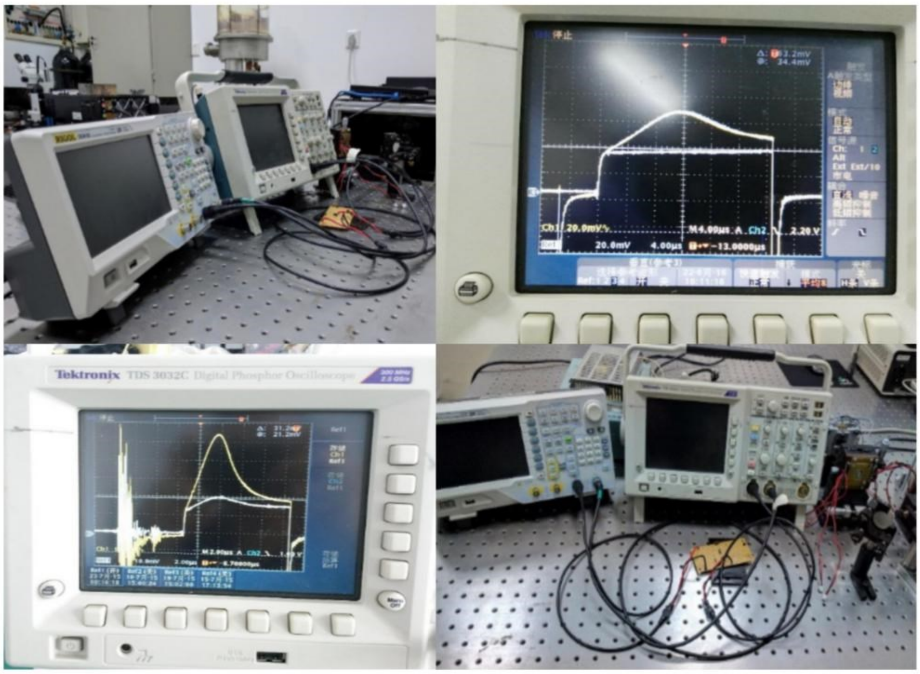

Figure S30. The photos for the photo-CELIV technology system.

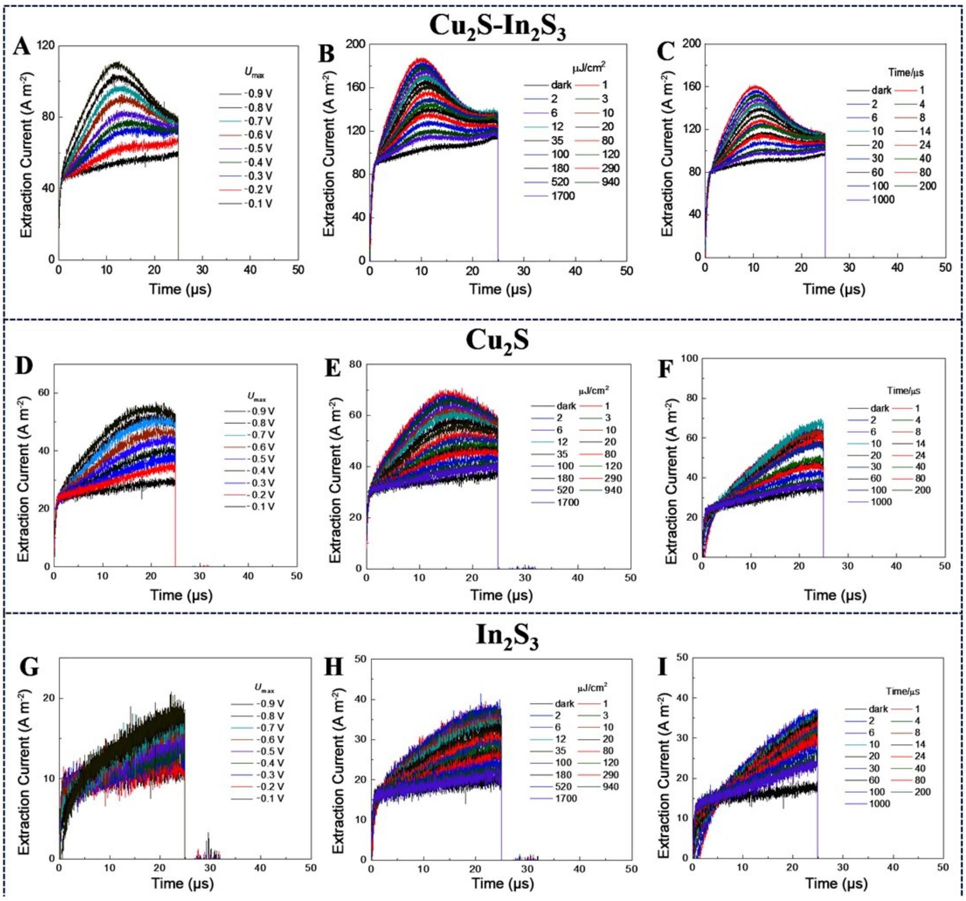

Figure S31. The original measured photo-CELIV curves for A) Cu_2S-In_2S_3, D) Cu_2S and G) In_2S_3 at various applied voltage pulse with different maximum. U_{offset} = -0.6V, t_{del}= 5 µs, light pulse = 80 µJ cm^{-2}. The original measured photo-CELIV curves for B) Cu_2S-In_2S_3, E Cu_2S and H) In_2S_3 at Various incident laser intensities at fixed t_{del}= 5 µs and the voltage pulse U_{max} = 0.6 V, U_{offset} = -0.6 V. The original measured photo-CELIV curves for C) Cu_2S-In_2S_3, F) Cu_2S and I) In_2S_3 at various delay times (t_{del}) between the light pulse = 80 µJ cm^{-2} and the voltage pulse U_{max} = 0.6 V, U_{offset} = -0.6 V.

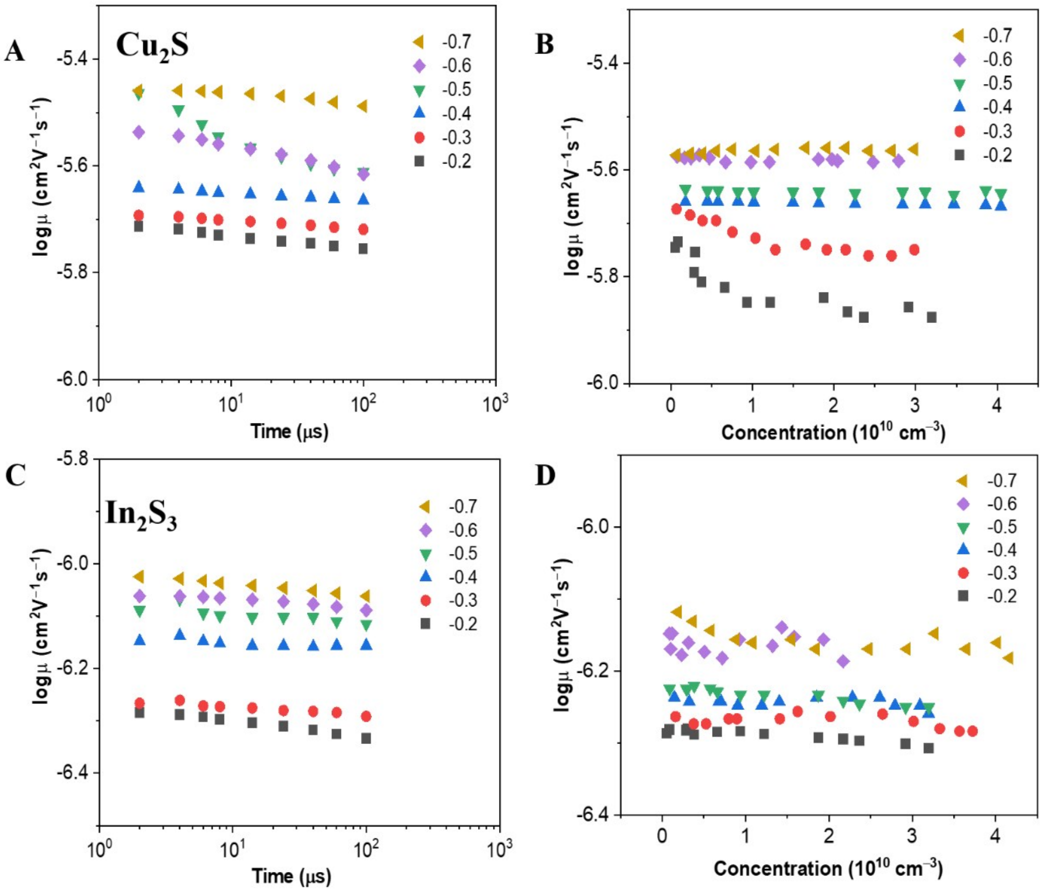

Figure S32. A) Carrier mobility of extracted charge carriers versus the delay time at fixed t_{del}= 5 µs for Cu_2S, which is detected at different applied voltage U_{offset} = -0.6V. B) Carrier mobility of Cu_2S versus the concentration of the extracted charge carriers calculated from light intensity dependent measurement at fixed t_{del} = 5 µs, U_{offset} = -0.6V. C) Carrier mobility of extracted charge carriers versus the delay time at fixed t_{del}= 5 µs for In_2S_3, which is detected at different applied voltage U_{offset} = -0.6V. D) Carrier mobility of In_2S_3 versus the concentration of the extracted charge carriers calculated from light intensity dependent measurement at fixed t_{del} = 5 µs, U_{offset} = -0.6V.

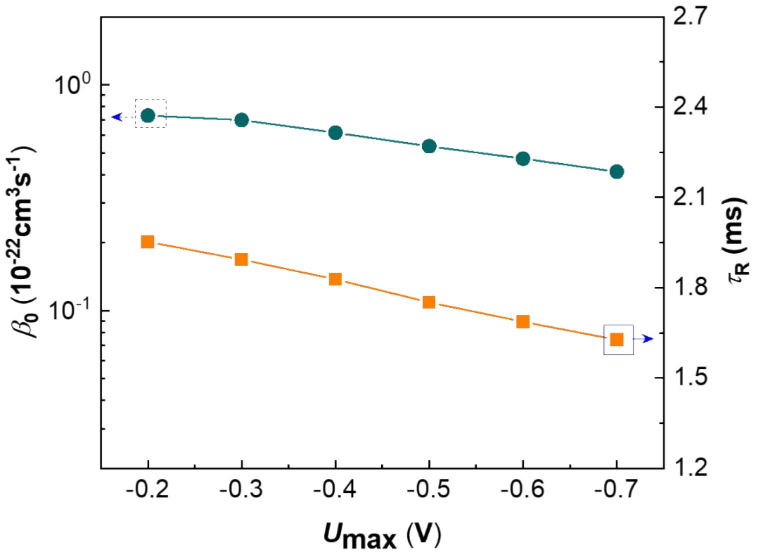

Figure S33. The fitted value of τ_R and β_0 at different voltage for Cu_2S-In_2S_3 heterostructure.

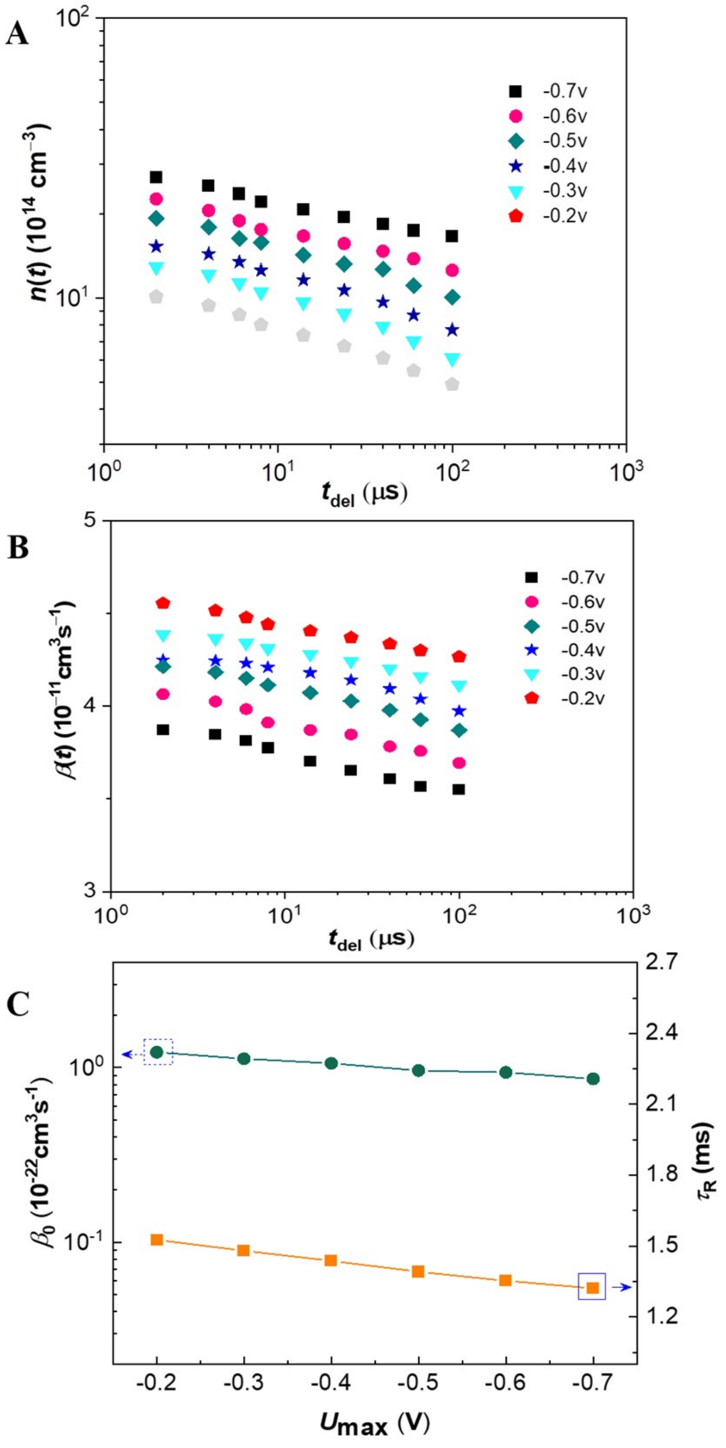

Figure S34. A) Concentration of extracted charge carriers for Cu_2S versus the delay time, which is detected at different applied voltage. B) Time-dependent recombination coefficient of Cu_2S. C) The fitted value of τ_R and β_0 at different voltage.

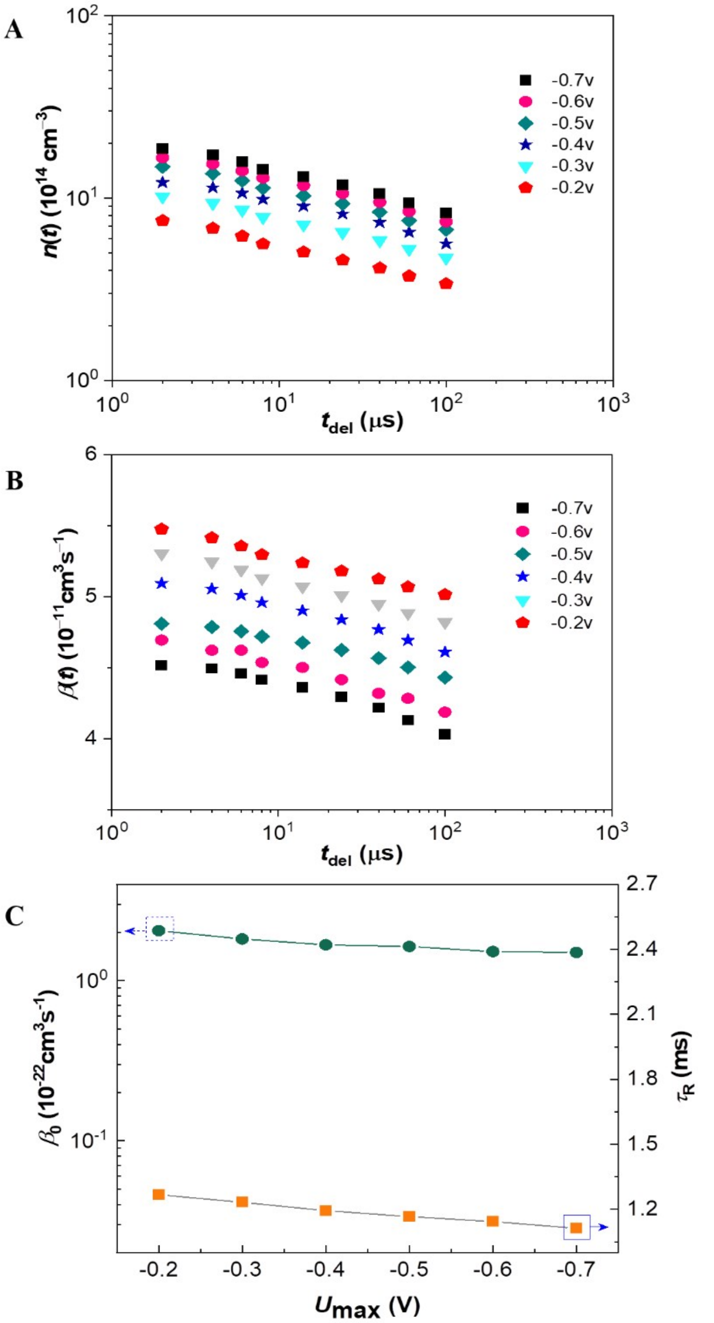

Figure S35. A) Concentration of extracted charge carriers for In_2S_3 versus the delay time, which is detected at different applied voltage. B) Time-dependent recombination coefficient of In_2S_3. C) The fitted value of τ_R and β_0 at different voltage.

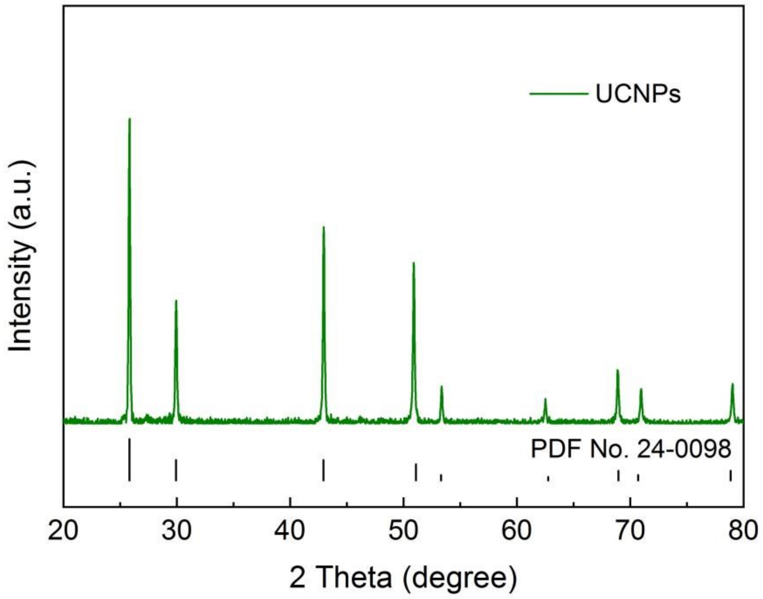

Figure S36. XRD pattern for $BaGdF_5$: 30%Yb^{3+}, 5%Er^{3+} material.

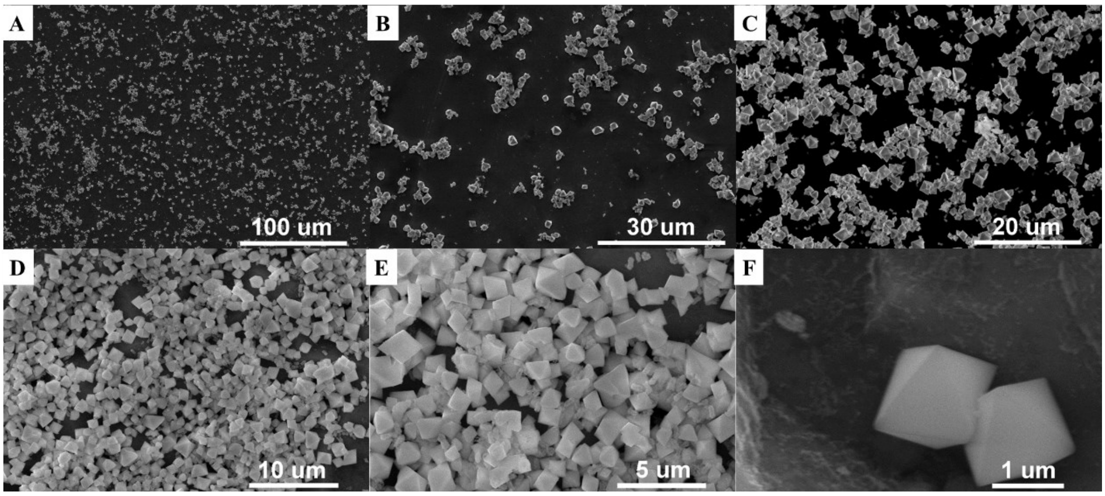

Figure S37. SEM images for $BaGdF_5$: $30\%Yb^{3+}$, $5\%Er^{3+}$ material.

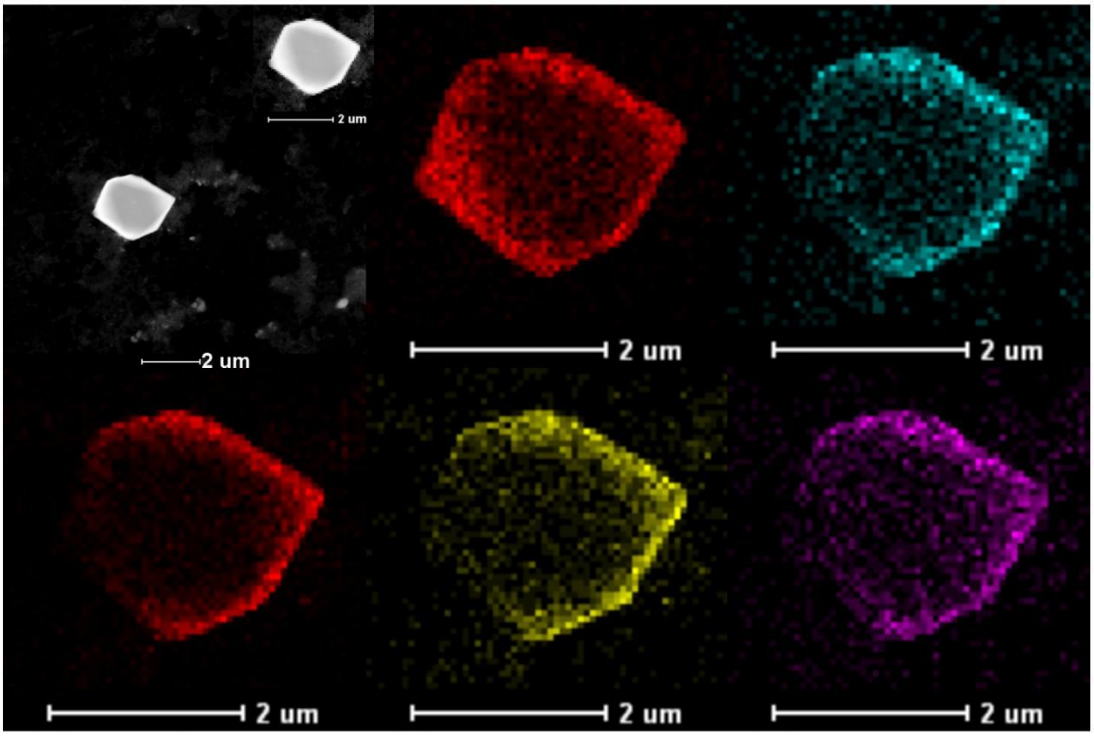

Figure S38. TEM images for $BaGdF_5$: 30%Yb^{3+}, 5%Er^{3+} material and the corresponding mapping images.

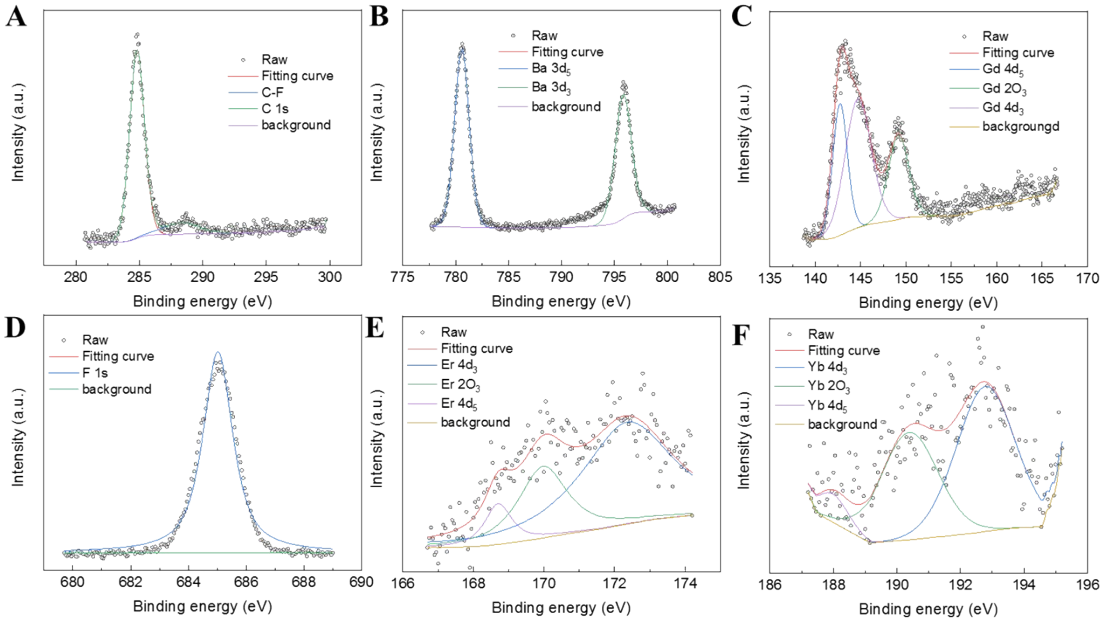

Figure S39. XPS spectra for $BaGdF_5$: 30%Yb^{3+}, 5%Er^{3+} material.

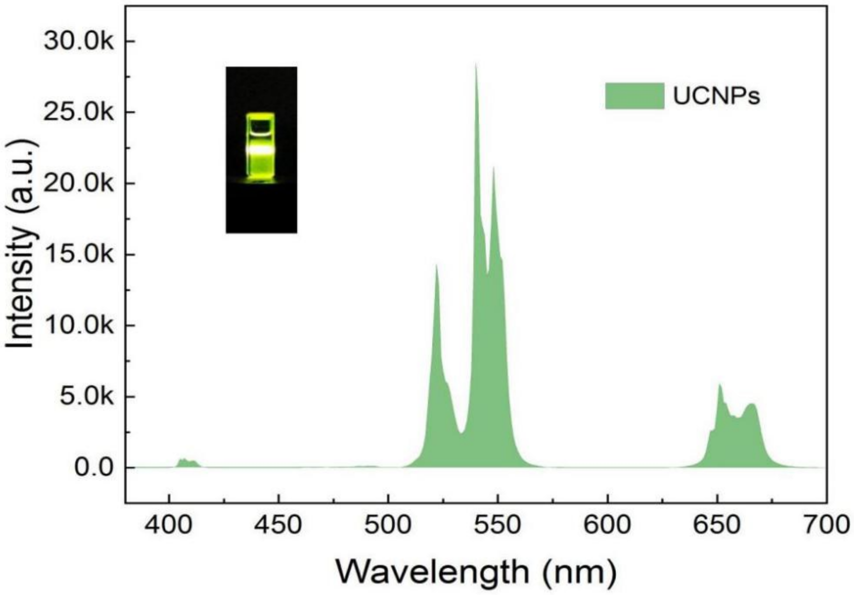

Figure S40. Photoluminescence emission curves of the $BaGdF_5$: 30%Yb^{3+}, 5%Er^{3+} sample and the inset show the corresponding photo.

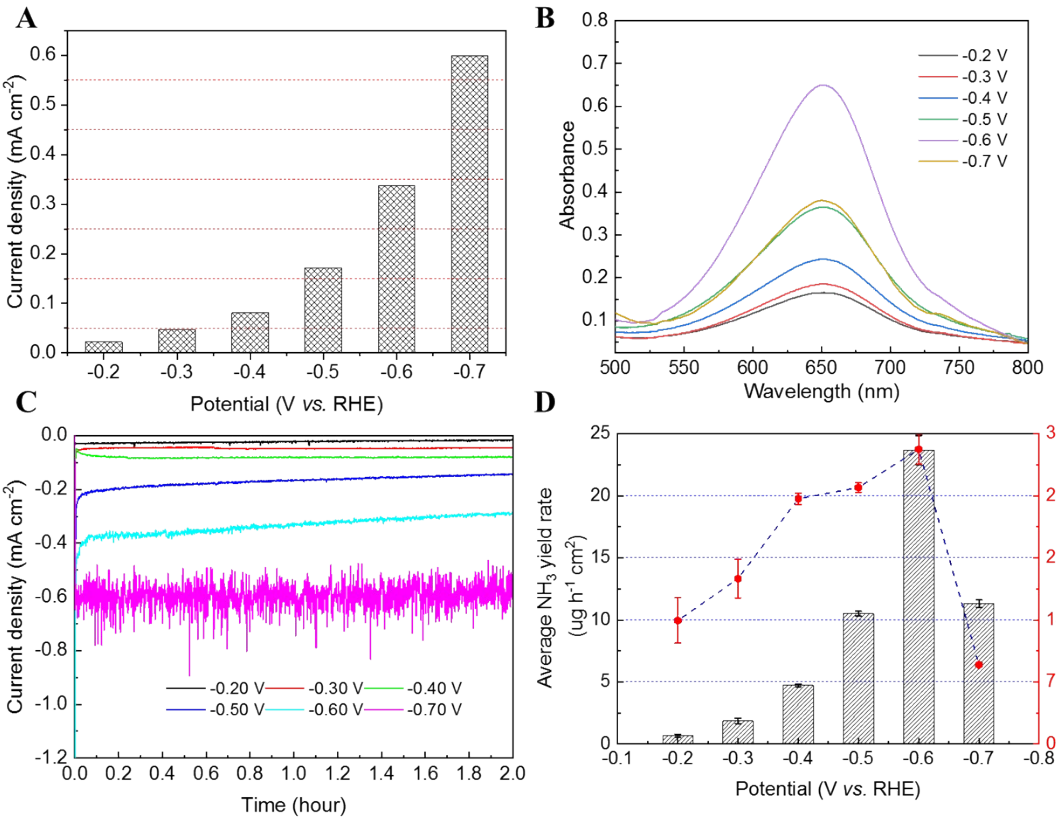

Figure S41. A) The current densities for Cu_2S-In_2S_3-UCNPs electrolyzed at different applied potentials under one sunlight. B) UV-Vis curves of indophenol assays with NH_4^+ ions for Cu_2S-In_2S_3-UCNPs electrolyzed at different applied potentials after incubated for 2 h at room temperature. C) Chrono-amperometry results at the corresponding potentials. D) Yield rates of NH_3 (black bar) and Faradaic efficiencies (red point) at each given potential for Cu_2S-In_2S_3-UCNPs catalyst.

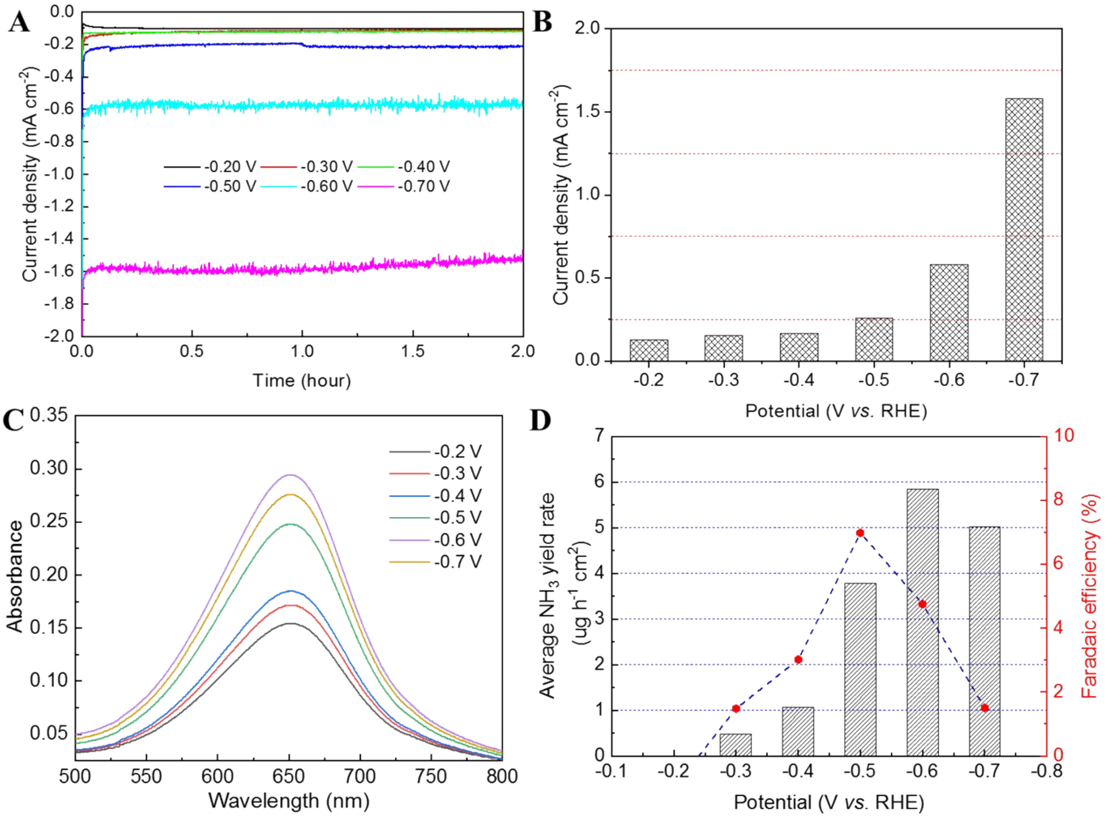

Figure S42. A) Chrono-amperometry results at the corresponding potentials. B) The current densities for physically mixed Cu_2S-In_2S_3 and UCNPs electrolyzed at different applied potentials under one sunlight. C) UV-Vis curves of indophenol assays with NH_4^+ ions for physically mixed Cu_2S-In_2S_3 and UCNPs electrolyzed at different applied potentials after incubated for 2 h at room temperature. D) Yield rates of NH_3 (black bar) and Faradaic efficiencies (red point) at each given potential for physically mixed Cu_2S-In_2S_3 and UCNPs catalyst.

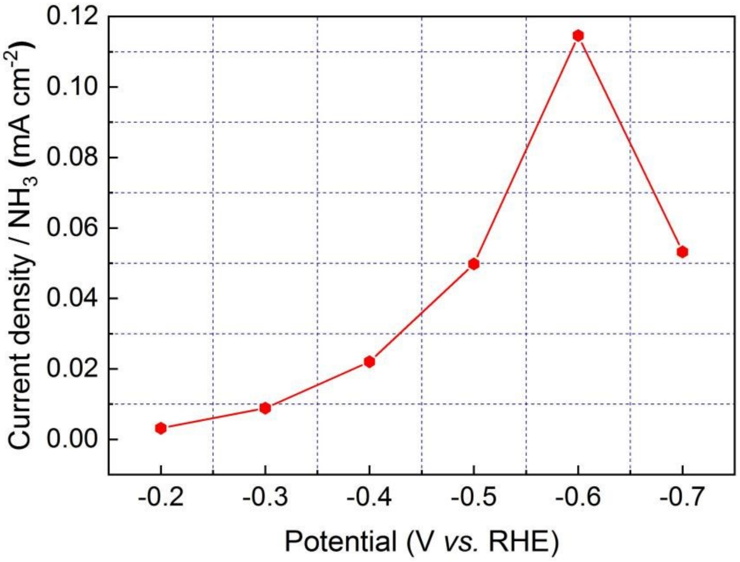

Figure S43. The current densities of Cu_2S-In_2S_3-UCNPs catalyst for producing ammonia at different applied potential under one sunlight.

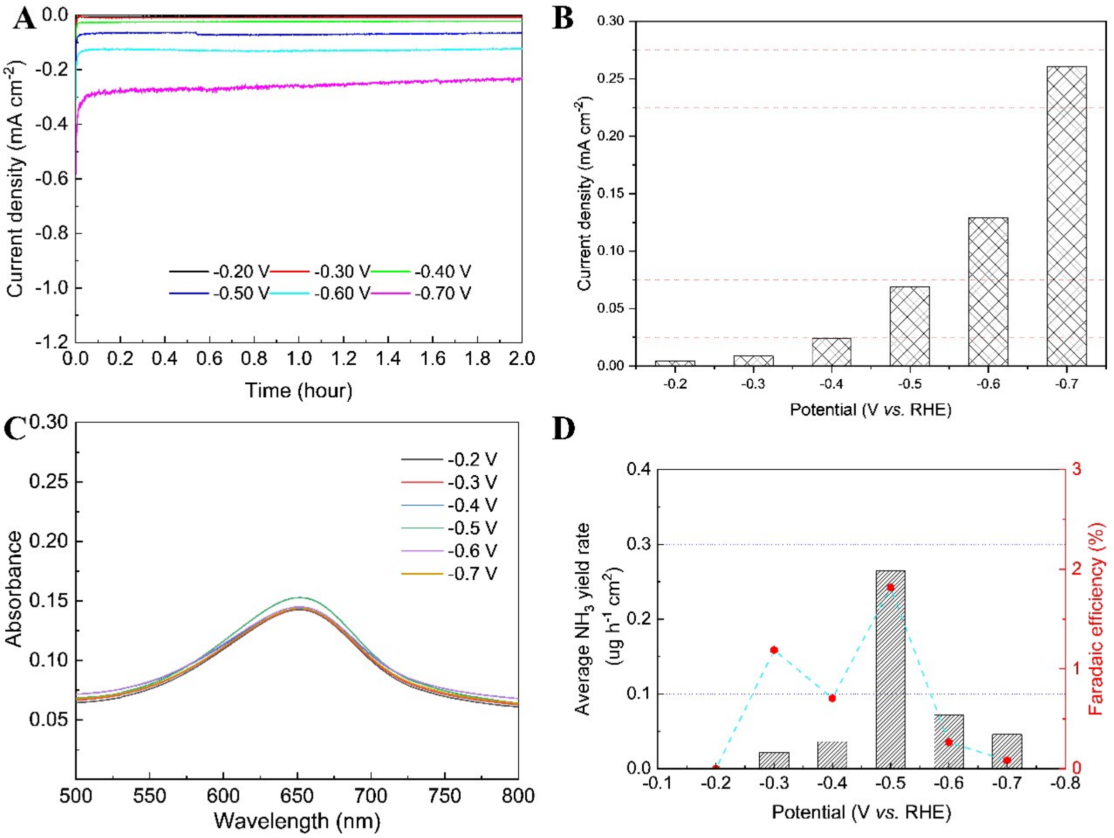

Figure S44. A) Chrono-amperometry results at the corresponding potentials. B) The current densities for UCNPs electrolyzed at different applied potentials under one sunlight. C) UV-Vis curves of indophenol assays with NH_4^+ ions for UCNPs electrolyzed at different applied potentials after incubated for 2 h at room temperature. D) Yield rates of NH_3 (black bar) and Faradaic efficiencies (red point) at each given potential for UCNPs catalyst.

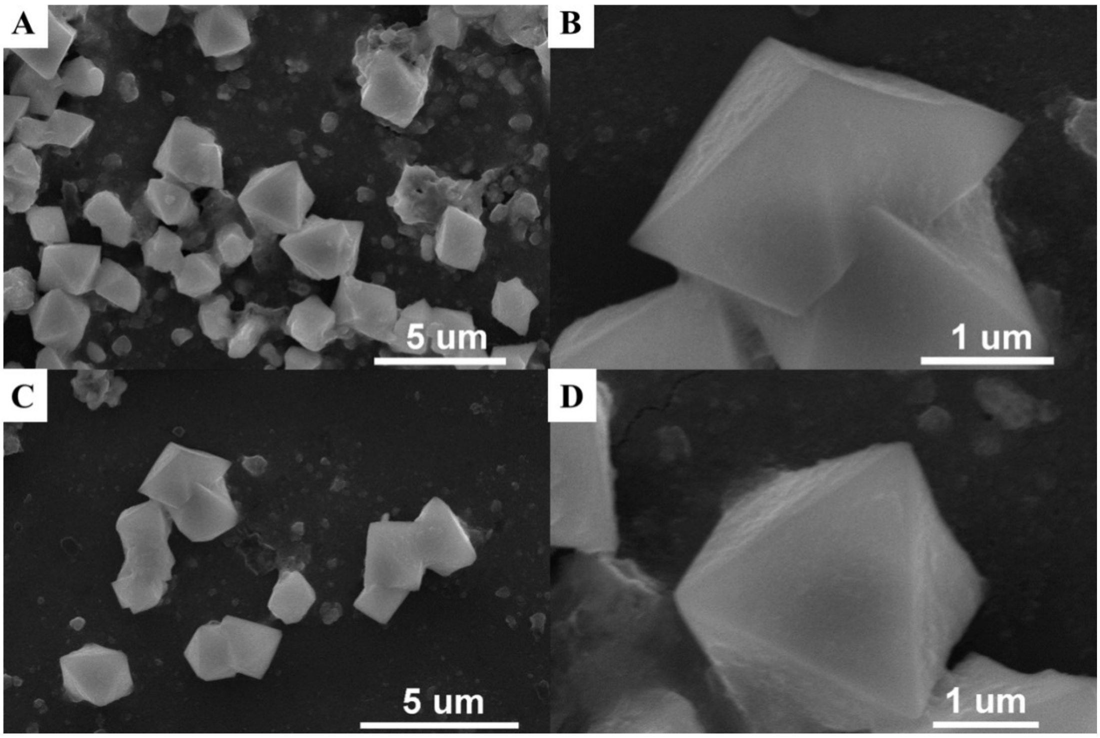

Figure S45. SEM images for $BaGdF_5$: 30%Yb^{3+}, 5%Er^{3+} material after reaction.

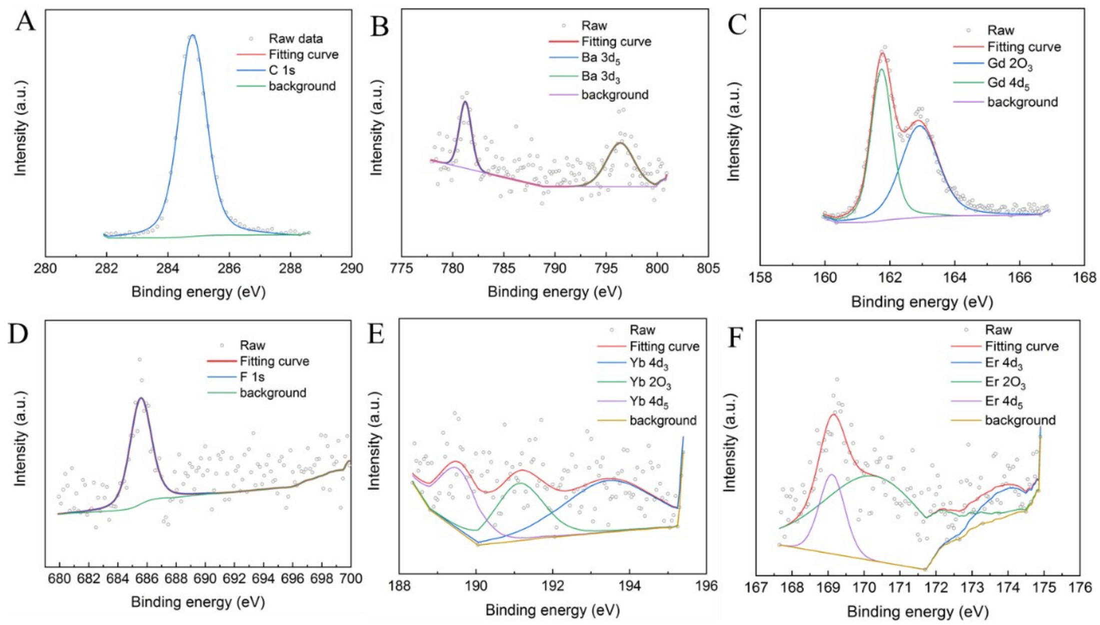

Figure S46. XPS spectra for $BaGdF_5$: 30%Yb^{3+}, 5%Er^{3+} material after reaction.

Supplemental Tables

Table 1. Comparison of heterogeneous catalysts for photo(electro)catalytic N_2 reduction.

Year	Catalyst	Scavenger	Light source	Ammonia Generation rate	Ammonia Detection methods	Reference
Before 2017	CdS/Pt	None	UV	3.26 μmol g^{-1} h^{-1}	Nessler's reagent	3
	0.2 wt.% Fe-doped TiO_2	None	UV	11.5 μmol g^{-1} h^{-1}	Indophenol blue method	4
	B-doped diamond	None	UV	1.8 μg h^{-1}	Indophenol blue method	5
	Au NPs/$NbSrTiO_3$/Ru	Ethanol	550-800 nm	1100 μmol g^{-1} cm^{-2}	Indophenol blue method	6
	$BaTiO_3$	None	UV	0.87 μmol g^{-1} h^{-1}	Nessler's reagent	7
	BiOBr-001-O_V	None	$\lambda > 420$ nm	104.2 μmol g^{-1} h^{-1}	Nessler's reagent	8
	C-modified WO_3•H_2O	None	Full Spectrum	205 μmol g^{-1} h^{-1}	Nessler's reagent	9
	BiOCl	Methanol	Full Spectrum	92.4 μmol g^{-1} h^{-1}	Nessler's reagent	10
	Bi_5O_7Br	None	$\lambda > 400$ nm	1380 μmol g^{-1} h^{-1}	Nessler's reagent	11
	GNP/Bsi/Cr	Na_2SO_3	Full Spectrum	13.3 mg m^{-2} h^{-1}	Indophenol blue method, ammonia/ammonium ISE	12
	CuCr-LDH	None	Full Spectrum	78.6 μmol g^{-1} h^{-1}	Nessler's reagent	13
	CdS:MoFe protein	HEPES	$\lambda = 405$ nm	315 μmol g^{-1} min^{-1}	Biovision, fluorescence assay	14
After 2017	Au/TiO_2-V_o	Methanol	Full Spectrum	78.6 μmol g^{-1} h^{-1}	Indophenol blue method	15
	Cu-doped TiO_2	None	Full Spectrum	78.9 μmol g^{-1} h^{-1}	Ion chromatography	16
	Au/end-CeO_2	Methanol	808 nm laser	114.3 μmol g^{-1} h^{-1}	Indophenol blue method	17
	TiO_2/Au/a-TiO_2	None	Full Spectrum	13.4 nmol cm^{-2} h^{-1}	Indophenol blue method	18
	Au-PTFE/TS	Na_2SO_3	Full Spectrum	18.9 mg cm^{-2} h^{-1}	indophenol blue method/ ammonia-	19

					ammonium ISE	
	Mo-doped $W_{18}O_{49}$	None	Full Spectrum	3.324 mg h^{-1} g$^{-1}{}_{cat}$	Nessler’s reagent	20
	BPCNS	methanol	>420 nm	9.846 mg h^{-1} g$^{-1}{}_{cat}$	Nessler’s reagent	21
	g-C_3N_4/Cs_xWO_3	methanol	Full spectrum	5.627 mg h^{-1} g$^{-1}{}_{cat}$	Nessler’s reagent	22

Table 2. Comparison of heterogeneous catalysts for electrocatalytic N_2 reduction.

Year	Catalyst	Electrolyte	Faradaic Efficiency	Ammonia Generation rate	Ammonia Detection methods	Reference
			(V vs. RHE)			
Before 2019	Tetrahexahedral Au	0.1 M KOH	4.0%	16.48 mg h^{-1} m^{-2}	Nessler's reagent	23
	a-Au/CeOx–RGO	0.1 M HCl	10.10%	8.3 mg h^{-1} g^{-1}_{cat}	Indophenol blue method	24
	Au cluster/TiO_2	0.1 M HCl	8.11%	21.4 mg h^{-1} g^{-1}_{cat}	Indophenol blue method	25
	Fe_2O_3/CNT	Gas-phase reaction	0.14% (-1.0 V vs Ag/AgCl)	2.2 mg h^{-1} m^{-2} (-2.0 vs Ag/ AgCl)	salicylic acid method, ammonia/ammonium ISE	26
	PCN	0.1 M HCl	11.59%	8.09 mg h^{-1} g^{-1}_{cat}	Indophenol blue method	27
	B-doped graphene	0.05 M H_2SO_4	10.8%	98 mg h^{-1} m^{-2}	Indophenol blue method	28
	N-doped porous carbon	0.05 M H_2SO_4	-	23.8 mg h^{-1} g^{-1}_{cat}	Nessler's reagent	29
	Mo_2N nanorod	0.1 M HCl	4.5%	78.4 mg h^{-1} g^{-1}_{cat}	Indophenol blue method	30
	Au SAs-N-doped porous carbons	0.1 M HCl	22%	360 mg h^{-1} m^{-2}	Indophenol blue method	31
	Ru SACs/N-C	0.05 M H_2SO_4	29.6%	120.9 mg h^{-1} g^{-1}_{cat}	Indophenol blue method, IC	32
	a-$Bi_4V_2O_{11}$/CeO_2	0.1 M HCl	10.16%	23.21 mg h^{-1} g^{-1}_{cat}	Indophenol blue method	33
After 2019	hierarchical porous MoN@NC	0.1 M HCl	6.9%	76.9 µg h^{-1} mg^{-1}	Indophenol blue method	34
	CuO NWAs	0.2 M Na_2SO_4	95.8%	0.245 mmol h^{-1} cm^{-2}	NMR/colorimetric methods	35
	$Ni_xZn_{(1-x)}$BMOF	0.1 M KOH	21%	115 µg cm^{-2} h^{-1}	Nessler's reagent	36
	Au_1Cu_1	0.05 M H_2SO_4	54.96%	154.91 µg h^{-1} mg_{cat}^{-1}	Indophenol blue method	37
	S-rich MoS_2	0.1 M Li_2SO_4	9.81%	43.4 µg h^{-1} mg^{-1}	indophenol blue method	38
	p-Fe_2O_3/CC	0.1 M Na_2SO_4	7.69%	6.78 µg h^{-1} cm^{-2}	indophenol blue method	39
	AuPdP NWs	0.1 M Na_2SO_4	15.44%	7.51 µg h^{-1} cm^{-2}	indophenol blue method	40

Table 3. Photovoltaic performance of Cu_2S-In_2S_3, Cu_2S and In_2S_3 photovoltage devices.

Device	V_{oc}/V	V_{eff}/V	J_{sc}/mA cm^{-2}	FF/%	PCE/%
In_2S_3	0.61	0.6057	5.02	42.3	1.29
Cu_2S	0.70	0.6949	9.51	53	3.52
Cu_2S-In_2S_3	0.75	0.7497	16.05	69	8.31

Supplemental References

1. Aayush, R. S. et al. (2019). Strategies toward Selective Electrochemical Ammonia Synthesis. ACS Catal. *9*, 8316-8324.
2. Zhang, M. Y. et al. (2019). Reconfiguration of interfacial energy band structure for high-performance inverted structure perovskite solar cells. Nat. Commun. *10*, 4593.
3. Miyama, H., Fujii, N., Nagae, Y. (1980). Heterogeneous photocatalytic synthesis of ammonia from water and nitrogen. Chem. Phys. Lett. *74*, 523-524.
4. Schrauzer, G. N., Guth, T. D. (1977). Photolysis of water and photoreduction of nitrogen on titanium dioxide. J. Am. Chem. Soc. *99*, 7189-7193.
5. Zhu, D., Zhang, L., Ruther, R. E., Hamers, R. J. (2013). Photo-illuminated diamond as a solid-state source of solvated electrons in water for nitrogen reduction. Nat. Mater. *12*, 836-841.
6. Oshikiri, T., Ueno, K., Misawa, H. (2014). Plasmon-induced ammonia synthesis through nitrogen photofixation with visible light irradiation. Angew. Chem. Int. Ed. *53*, 9802-9805.
7. Li, Q., Domen, K., Naito, S., Onishi, T., Tamaru, K. (1983). Photocatalytic synthesis and photodecomposition of ammonia over $SrTiO_3$ and $BaTiO_3$ based catalysts. Chem. Lett. *12*, 321-324.
8. Li, H., Shang, J., Ai, Z., Zhang, L. (2015). Efficient visible light nitrogen fixation with BiOBr nanosheets of oxygen vacancies on the exposed {001} facets. J. Am. Chem. Soc. *137*, 6393-6399.
9. Li, X., Wang, W., Jiang, D., Sun, S., Zhang, L., Sun, X. (2016). Efficient solar-driven nitrogen fixation over carbon-tungstic-acid hybrids. Chem. Eur. J. *22*, 13819-13822.
10. Li, H., Shang, J., Shi, J., Zhao, K., Zhang, L. (2016). Facet-dependent solar ammonia synthesis of BiOCl nanosheets via a proton-assisted electron transfer pathway. Nanoscale *8*, 1986-1993.
11. Wang, S., Hai, X., Ding, X., Chang, K., Xiang, Y., Meng, X., Yang, Z., Chen, H., Ye, J. (2017). Light-switchable oxygen vacancies in ultrafine Bi_5O_7Br nanotubes for boosting solar-driven nitrogen fixation in pure water. Adv. Mater. *29*, 1701774.
12. Ali, M., Zhou, F., Chen, K., Kotzur, C., Xiao, C., Bourgeois, L., Zhang, X., MacFarlane, D. R. (2016). Nanostructured photoelectrochemical solar cell for nitrogen reduction using plasmon-enhanced black silicon. Nat. Commun. *7*, 11335.
13. Wang, Y. J., Wei, W. S., Li, M. Y., Hu, S. Z., Zhang, J., Feng, R. J. (2017). In situ construction of Z-scheme g-C_3N_4/$Mg_{1.1}Al_{0.3}Fe_{0.2}O_{1.7}$ nanorod heterostructures with high N_2 photofixation ability under visible light. RSC Adv. *7*, 18099-18107.
14. Brown, K. A., Harris, D. F., Wilker, M. B., Rasmussen, A., Khadka, N., Hamby, H., Keable, S., Dukovic, G., Peters, J. W., Seefeldt, L. C., et al. (2016). Light-driven dinitrogen reduction catalyzed by a CdS:nitrogenase MoFe protein biohybrid. Science *352*, 448-450.
15. Yang, J., Guo, Y., Jiang, R., Qin, F., Zhang, H., Lu, W., Wang, J., Yu, J. C. (2018). High-efficiency "working-in-tandem" nitrogen photofixation achieved by assembling plasmonic gold nanocrystals on ultrathin titania nanosheets. J. Am. Chem. Soc. *140*, 8497-8508.
16. Zhao, Y., Zhao, Y., Shi, R., Wang, B., Waterhouse, G. I. N., Wu, L. Z., Tung, C. H., Zhang, T. (2019). Tuning oxygen vacancies in ultrathin TiO_2 nanosheets to boost photocatalytic nitrogen fixation up to 700 nm. Adv. Mater. *31*, 1806482.
17. Jia, H., Du, A., Zhang, H., Yang, J., Jiang, R., Wang, J., Zhang, C. Y. (2019). Site-selective growth of crystalline ceria with oxygen vacancies on gold nanocrystals for near-infrared nitrogen photofixation. J. Am. Chem. Soc. *141*, 5083-5086.
18. Li, C., Wang, T., Zhao, Z.-J., Yang, W., Li, J.-F., Li, A., Yang, Z., Ozin, G. A., Gong, J. (2018). Promoted fixation of molecular nitrogen with surface oxygen vacancies on plasmon-enhanced TiO_2 photoelectrodes. Angew. Chem. Int. Ed. *57*, 5278-5282.
19. Zheng, J. Y. et al. (2019). Photoelectrochemical Synthesis of Ammonia on the Aerophilic-Hydrophilic Heterostructure with 37.8% Efficiency. Chem *5*, 617-633.
20. Zhang, N. et al. (2018). Refining Defect States in $W_{18}O_{49}$ by Mo Doping: A Strategy for Tuning N_2 Activation towards Solar-Driven Nitrogen Fixation. J. Am. Chem. Soc. *140(30)*, 9434-9443.
21. Qiu, P. et al. (2018). Metal-free black phosphorus nanosheets-decorated graphitic carbon nitride nanosheets with CP bonds for excellent photocatalytic nitrogen fixation. Appl. Catal., B *221*, 27-35.
22. Shi, A. et al. (2018). Photocatalytic NH_3 versus H_2 evolution over g-C_3N_4/Cs_xWO_3: O_2 and methanol tipping the scale. Appl. Catal., B *235*, 197-206.
23. Bao, D. et al. (2017). Electrochemical Reduction of N_2 under Ambient Conditions for Artificial N_2 Fixation and Renewable Energy Storage Using N_2/NH_3 Cycle. Adv. Mater. *29*, 1604799.

24. Li, S. J. et al. (2017). Amorphizing of Au Nanoparticles by CeO_x-RGO Hybrid Support towards Highly Efficient Electrocatalyst for N_2 Reduction under Ambient Conditions. Adv. Mater. *29*, 1700001.
25. Shi, M. M. et al. (2017). Au Sub-Nanoclusters on TiO_2 toward Highly Efficient and Selective Electrocatalyst for N_2 Conversion to NH_3 at Ambient Conditions. Adv. Mater. *29*, 1606550.
26. Chen, S. et al. (2017). Electrocatalytic Synthesis of Ammonia at Room Temperature and Atmospheric Pressure from Water and Nitrogen on a Carbon-Nanotube-Based Electrocatalyst. Angew. Chem. Int. Ed. *56*, 2699-2703.
27. Lv, C. et al. (2018). Defect Engineering Metal-Free Polymeric Carbon Nitride Electrocatalyst for Effective Nitrogen Fixation under Ambient Conditions. Angew. Chem. Int. Ed. *57*, 10246-10250.
28. Yu, X. et al. (2018). Boron-Doped Graphene for Electrocatalytic N_2 Reduction. Joule *2*, 1610-1622.
29. Liu, Y. et al. (2018). Facile Ammonia Synthesis from Electrocatalytic N_2 Reduction under Ambient Conditions on N-Doped Porous Carbon. ACS Catal. *8*, 1186-1191.
30. Ren, X. et al. (2018). Electrochemical N_2 fixation to NH_3 under ambient conditions: Mo_2N nanorod as a highly efficient and selective catalyst. Chem. Commun. *54*, 8474-8477.
31. Wang, H. et al. (2018). Ambient Electrosynthesis of Ammonia: Electrode Porosity and Composition Engineering. Angew. Chem. Int. Ed. *57*, 12360-12364.
32. Geng, Z. et al. (2018). Achieving a Record-High Yield Rate of 120.9 μg_{NH3} mg_{cat}^{-1} h^{-1} for N_2 Electrochemical Reduction over Ru Single-Atom Catalysts. Adv. Mater. *30*, 1803498.
33. Lv, C. et al. (2018). An Amorphous Noble-Metal-Free Electrocatalyst that Enables Nitrogen Fixation under Ambient Conditions. Angew. Chem. Int. Ed. *57*, 6073-6076.
34. Yang, X. H. et al. (2019). Insights into the role of cation vacancy for significantly enhanced electrochemical nitrogen reduction. Appl. Catal., B *264*, 118477.
35. Wang, Y. T. et al. (2020). Unveiling the Activity Origin of a Copper-based Electrocatalyst for Selective Nitrate Reduction to Ammonia. Angew. Chem. Int. Ed. *59*, 5350-5354.
36. Mukherjee, S. et al. Atomically Dispersed Single Ni Site Catalysts for Nitrogen Reduction toward E lectrochemical Ammonia Synthesis Using N_2 and H_2O. *Small Methods* 1900821 (2020).
37. Liu, Y. Q. et al. (2020). Coupling Cu with Au for enhanced electrocatalytic activity of nitrogen reduction reaction. Nanoscale *12*, 1811-1816.
38. Liu, Y. Y. et al. (2019). Ambient Ammonia Electrosynthesis: Dramatically Enhanced Ambient Ammonia Electrosynthesis Performance by In-Operando Created Li-S Interactions on MoS_2 Electrocatalyst. Adv. Energy Mater. *9*, 1970042.
39. Wang, Z. Q. et al. (2019). Electrocatalytic Nitrogen Reduction to Ammonia by Fe_2O_3 Nanorod Array on Carbon Cloth. ACS Sustainable Chem. Eng. *7*, 11754-11759.
40. Wang, H. J. et al. (2019). Metal-Nonmetal One-Dimensional Electrocatalyst: AuPdP Nanowires for Ambient Nitrogen Reduction to Ammonia. ACS Sustainable Chem. Eng. *7*, 15772-15777.